

## RESEARCH ARTICLE SUMMARY

## OUTER SOLAR SYSTEM

## The geology and geophysics of Kuiper Belt object (486958) Arrokoth

J. R. Spencer *et al.*

**INTRODUCTION:** On 1 January 2019, the New Horizons spacecraft passed 3538 km from Kuiper Belt object (KBO) (486958) Arrokoth. Arrokoth is a contact binary consisting of two distinct lobes, connected by a narrow neck. Its orbital parameters, albedo, and color make Arrokoth a typical cold classical KBO (CCKBO). CCKBOs are the most dynamically and physically primitive population of small Solar System bodies known.

**RATIONALE:** Since the publication of initial results from the flyby, additional data have been downlinked and analyzed. This paper describes the resulting analysis of Arrokoth's shape, geological evolution, and satellite and ring constraints.

**RESULTS:** Improved stereo imaging constrains the object's shape and topography and allows us to generate a stereographic terrain model. Typical relief on both lobes (away from the neck region) is ~0.5 km or smaller.

Arrokoth's rotational period is  $15.92 \pm 0.02$  hours, with its rotational pole pointing to right ascension =  $317.5 \pm 1^\circ$ , declination =  $-24.9 \pm 1^\circ$ , J2000 equinox. The object consists

of two roughly ellipsoidal lobes with overall dimensions of 36 km by 20 km by 10 km. The maximum dimensions of the two lobes are 20.6 km by 19.9 km by 9.4 km and 15.4 km by 13.8 km by 9.8 km, with uncertainties of 0.5 km by 0.5 km by 2.0 km. The total volume is equal to a sphere of diameter  $18.3 \pm 1.2$  km, and the volume ratio of the two lobes is  $1.9 \pm 0.5$ . Global bulk density must be  $>290 \text{ kg m}^{-3}$  if the neck is not in tension. Assuming a bulk density of  $500 \text{ kg m}^{-3}$ , as measured for comets, the mean surface gravity is  $\sim 1 \text{ mm s}^{-2}$ , and the compressive strength of the neck must be  $>2.3 \text{ kPa}$ .

The two lobes are closely aligned. The maximum axis of inertia of the large lobe is aligned within  $<5^\circ$  of that of the small lobe. The equatorial planes of the two lobes are also almost coincident in space.

The small lobe's surface is marked by complex albedo patterns, often with sinuous margins and no detectable topographic signature, whereas the large lobe's surface is dominated by clusters of low dark hills superposed on brighter, smoother terrain. The large lobe's surface is divided into distinct subunits, which may represent smaller bodies that accreted to

form it, though the overall smoothness of the surface, and the youthful appearance of many boundaries, which are sometimes undetectable or cross-cut by clusters of hills, suggest a more complex postformation history. If the sub-

## ON OUR WEBSITE

Read the full article at <http://dx.doi.org/10.1126/science.aay3999>

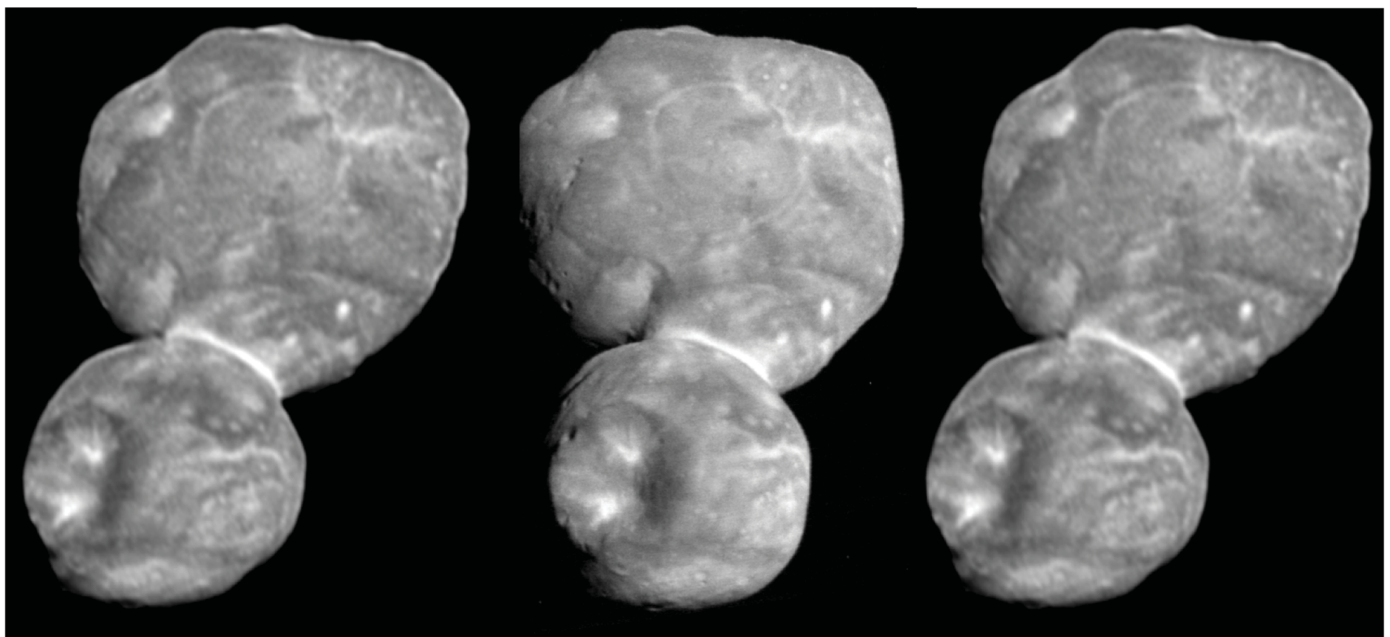
units did accrete first, the smoothness of their mutual boundaries suggests subsequent accretion of additional material and later reactivation of the boundaries.

We identify ~40 possible impact craters on Arrokoth, though only about 10 with high confidence. The largest crater, nicknamed Maryland, is about 7 km in diameter, and the rest are smaller than 1 km. Their size-frequency distribution is consistent with a single power law. Crater densities are lower than on many other small bodies but are consistent with a surface age of  $>4$  billion years. No satellites or rings are detected: Satellite diameter upper limit is 180 m out to 8000-km radius from Arrokoth.

**CONCLUSION:** Arrokoth's smooth, lightly cratered surface is unlike that of other Solar System bodies and appears to date from the period of planetary accretion. The alignment of its two lobes constrains the processes that formed this contact binary. Because its orbit, albedo, color, and rotation are typical of other CCKBOs, Arrokoth can likely be used to understand the cold classical belt as a whole. ■

The list of authors and their affiliations is available in the full article online.

\*Corresponding author. Email: [spencer@boulder.swri.edu](mailto:spencer@boulder.swri.edu)  
Cite this article as J. R. Spencer *et al.*, *Science* **367**, eaay3999 (2020). DOI: [10.1126/science.aay3999](https://doi.org/10.1126/science.aay3999)



**Stereo image pair of Arrokoth.** The left and center images can be viewed cross-eyed, or the right and center by direct viewing.

## RESEARCH ARTICLE

## OUTER SOLAR SYSTEM

# The geology and geophysics of Kuiper Belt object (486958) Arrokoth

J. R. Spencer<sup>1\*</sup>, S. A. Stern<sup>1</sup>, J. M. Moore<sup>2</sup>, H. A. Weaver<sup>3</sup>, K. N. Singer<sup>1</sup>, C. B. Olkin<sup>1</sup>, A. J. Verbiscer<sup>4</sup>, W. B. McKinnon<sup>5</sup>, J. Wm. Parker<sup>1</sup>, R. A. Beyer<sup>6,2</sup>, J. T. Keane<sup>7</sup>, T. R. Lauer<sup>8</sup>, S. B. Porter<sup>1</sup>, O. L. White<sup>6,2</sup>, B. J. Buratti<sup>9</sup>, M. R. El-Maarry<sup>10,11</sup>, C. M. Lisse<sup>3</sup>, A. H. Parker<sup>1</sup>, H. B. Throop<sup>12</sup>, S. J. Robbins<sup>1</sup>, O. M. Umurhan<sup>2</sup>, R. P. Binzel<sup>13</sup>, D. T. Britt<sup>14</sup>, M. W. Buie<sup>1</sup>, A. F. Cheng<sup>3</sup>, D. P. Cruikshank<sup>2</sup>, H. A. Elliott<sup>15</sup>, G. R. Gladstone<sup>15</sup>, W. M. Grundy<sup>16,17</sup>, M. E. Hill<sup>3</sup>, M. Horanyi<sup>18</sup>, D. E. Jennings<sup>19</sup>, J. J. Kavelaars<sup>20</sup>, I. R. Linscott<sup>21</sup>, D. J. McComas<sup>22</sup>, R. L. McNutt Jr.<sup>3</sup>, S. Protopapa<sup>1</sup>, D. C. Reuter<sup>19</sup>, P. M. Schenk<sup>23</sup>, M. R. Showalter<sup>6</sup>, L. A. Young<sup>1</sup>, A. M. Zangari<sup>1</sup>, A. Y. Abedin<sup>20</sup>, C. B. Beddingfield<sup>6</sup>, S. D. Benecchi<sup>24</sup>, E. Bernardoni<sup>18</sup>, C. J. Bierson<sup>25</sup>, D. Borncamp<sup>26</sup>, V. J. Bray<sup>27</sup>, A. L. Chaikin<sup>28</sup>, R. D. D'ingra<sup>29</sup>, C. Fuentes<sup>30</sup>, T. Fuse<sup>31</sup>, P. L. Gay<sup>24</sup>, S. D. J. Gwyn<sup>20</sup>, D. P. Hamilton<sup>32</sup>, J. D. Hofgartner<sup>9</sup>, M. J. Holman<sup>33</sup>, A. D. Howard<sup>34</sup>, C. J. A. Howett<sup>1</sup>, H. Karoji<sup>35</sup>, D. E. Kaufmann<sup>1</sup>, M. Kinczyk<sup>36</sup>, B. H. May<sup>37</sup>, M. Mountain<sup>38</sup>, M. Pätzold<sup>39</sup>, J. M. Petit<sup>40</sup>, M. R. Piquette<sup>18</sup>, I. N. Reid<sup>41</sup>, H. J. Reitsema<sup>42</sup>, K. D. Runyon<sup>3</sup>, S. S. Sheppard<sup>43</sup>, J. A. Stansberry<sup>41</sup>, T. Stryk<sup>44</sup>, P. Tanga<sup>45</sup>, D. J. Tholen<sup>46</sup>, D. E. Trilling<sup>17</sup>, L. H. Wasserman<sup>16</sup>

The Cold Classical Kuiper Belt, a class of small bodies in undisturbed orbits beyond Neptune, is composed of primitive objects preserving information about Solar System formation. In January 2019, the New Horizons spacecraft flew past one of these objects, the 36-kilometer-long contact binary (486958) Arrokoth (provisional designation 2014 MU<sub>69</sub>). Images from the flyby show that Arrokoth has no detectable rings, and no satellites (larger than 180 meters in diameter) within a radius of 8000 kilometers. Arrokoth has a lightly cratered, smooth surface with complex geological features, unlike those on previously visited Solar System bodies. The density of impact craters indicates the surface dates from the formation of the Solar System. The two lobes of the contact binary have closely aligned poles and equators, constraining their accretion mechanism.

**O**n 1 January 2019 at 05:33:22 Universal Time (UT) the New Horizons spacecraft flew past the Kuiper Belt object (KBO) (486958) Arrokoth (provisional designation 2014 MU<sub>69</sub>, previously nicknamed “Ultima Thule”), at a distance of 3538 km (1). Arrokoth is a contact binary consisting of two distinct lobes, connected by a narrow neck. On the basis of its orbital semi-major axis, low eccentricity and inclination (2), and albedo and color (1, 3), Arrokoth is classified as a member of the dynamically cold, nonreson-

nant cold classical KBO (CCKBO) population and is probably a member of the tight orbital clustering of CCKBOs known as the kernel (4). There is no known mechanism for transporting the majority of these objects onto these nearly circular orbits, so they are thought to have formed in situ and remained dynamically undisturbed since the formation of the Solar System. Owing to the low impact rates (5) and low temperatures in the Kuiper Belt, CCKBOs are also thought to be physically primitive bodies. Arrokoth’s equivalent spherical diam-

eter of 18 km (see below) makes it about 5.5 times smaller in diameter than a known break in the size-frequency distribution of CCKBOs at diameter ~100 km (6).

Initial results from this flyby (1) were based on early data downlinked from the spacecraft. Since then, additional data have been downlinked, including (i) the highest-resolution images from the flyby, taken with the narrow-angle Long-Range Reconnaissance Imager (LORRI) camera (7). These LORRI images have a pixel scale that is four times finer (33 m pixel<sup>-1</sup>) than the 130 m pixel<sup>-1</sup> of previously available Multicolor Visible Imaging Camera (MVIC) (8) images (1), though because of smear and a lower signal-to-noise ratio (SNR), the effective resolution of the LORRI images is only about two times better than that of the MVIC images. Other downlinked data include (ii) additional LORRI images from earlier approach epochs, with higher SNR than previously downlinked data; (iii) improved LORRI distant approach rotational coverage, constraining the shape and rotational parameters; and (iv) additional satellite and ring search data from LORRI and MVIC. See (9) for image-processing details. We describe Arrokoth’s shape, geological evolution, and satellite and ring constraints resulting from these additional data and from continued analysis of all downlinked data.

## Stereo imaging

A pair of LORRI images, designated CA04 and CA06 [Fig. 1A and table S1 (9)], provides improved stereo imaging to constrain the shape and topography of the close approach hemispheres of the two lobes. A stereographic terrain model derived from these images [data S1 (9)], is shown in Fig. 2. Topographic relief in the stereo model is ~0.5 km or less on both lobes (away from the neck region), similar to the 1.0- and 0.5-km relief seen in limb profiles of the large and small lobes, respectively (1). The stereo images (Fig. 1A) show additional topographic detail that is visible to the eye but

<sup>1</sup>Southwest Research Institute, Boulder, CO 80302, USA. <sup>2</sup>NASA Ames Research Center, Moffett Field, CA 94035-1000, USA. <sup>3</sup>Johns Hopkins University Applied Physics Laboratory, Laurel, MD 20723, USA. <sup>4</sup>Department of Astronomy, University of Virginia, Charlottesville, VA 22904, USA. <sup>5</sup>Department of Earth and Planetary Sciences and McDonnell Center for the Space Sciences, Washington University, St. Louis, MO 63130, USA. <sup>6</sup>SETI Institute, Mountain View, CA 94043, USA. <sup>7</sup>Division of Geological and Planetary Sciences, California Institute of Technology, Pasadena, CA 91125, USA. <sup>8</sup>National Science Foundation’s National Optical Infrared Astronomy Research Laboratory, Tucson, AZ 26732, USA. <sup>9</sup>Jet Propulsion Laboratory, California Institute of Technology Pasadena, CA 91109, USA. <sup>10</sup>Department of Earth and Planetary Sciences, Birkbeck, University of London, London WC1E 7HX, UK. <sup>11</sup>University College London, Gower St, Bloomsbury, London WC1E 6BT, UK. <sup>12</sup>Independent Consultant, Washington, D.C., USA. <sup>13</sup>Massachusetts Institute of Technology, Cambridge, MA 02139, USA. <sup>14</sup>Department of Physics, University of Central Florida, Orlando, FL 32816, USA. <sup>15</sup>Southwest Research Institute, San Antonio, TX 78238, USA. <sup>16</sup>Lowell Observatory, Flagstaff, AZ 86001, USA. <sup>17</sup>Department of Astronomy and Planetary Science, Northern Arizona University, Flagstaff, AZ, 86011, USA. <sup>18</sup>Laboratory for Atmospheric and Space Physics, University of Colorado, Boulder, CO 80303, USA. <sup>19</sup>NASA Goddard Space Flight Center, Greenbelt, MD 20771, USA. <sup>20</sup>National Research Council of Canada, Victoria, BC V9E 2E7, Canada. <sup>21</sup>Independent Consultant, Mountain View, CA 94043, USA. <sup>22</sup>Department of Astrophysical Sciences, Princeton University, Princeton, NJ 08544, USA. <sup>23</sup>Lunar and Planetary Institute, Houston, TX 77058, USA. <sup>24</sup>Planetary Science Institute, Tucson, AZ 85719, USA. <sup>25</sup>Earth and Planetary Science Department, University of California, Santa Cruz, CA 95064, USA. <sup>26</sup>Decipher Technology Studios, Alexandria, VA 22314, USA. <sup>27</sup>Lunar and Planetary Laboratory, University of Arizona, Tucson, AZ 85721, USA. <sup>28</sup>Independent Science Writer, Arlington, VT 05250, USA. <sup>29</sup>University of Idaho, Moscow, ID 83844, USA. <sup>30</sup>Universidad de Chile, Centro de Astrofísica y Tecnologías Afines, Santiago, Chile. <sup>31</sup>Kashima Space Technology Center, National Institute of Information and Communications Technology, Kashima, Ibaraki 314-8501, Japan. <sup>32</sup>Department of Astronomy, University of Maryland, College Park, MD 20742, USA. <sup>33</sup>Center for Astrophysics, Harvard-Smithsonian Center for Astrophysics, Cambridge, MA 02138, USA. <sup>34</sup>Department of Environmental Sciences, University of Virginia, Charlottesville, VA 22904, USA. <sup>35</sup>National Institutes of Natural Sciences, Tokyo, Japan. <sup>36</sup>Marine, Earth, and Atmospheric Sciences, North Carolina State University, Raleigh, NC 27695, USA. <sup>37</sup>Independent Collaborator, Windlesham GU20 6YW, UK. <sup>38</sup>Association of Universities for Research in Astronomy, Washington, DC 20004, USA. <sup>39</sup>Rheinisches Institut für Umweltforschung an der Universität zu Köln, Cologne 50931, Germany. <sup>40</sup>Institut Univers, Temps-fréquence, Interfaces, Nanostructures, Atmosphère et environnement, Molécules, Unité Mixte de Recherche, Centre National de la Recherche Scientifique, Université Bourgogne Franche Comte, F-25000 Besançon, France. <sup>41</sup>Space Telescope Science Institute, Baltimore, MD 21218, USA. <sup>42</sup>Independent Consultant, Holland, MI 49424, USA. <sup>43</sup>Department of Terrestrial Magnetism, Carnegie Institution for Science, Washington, DC 20015, USA. <sup>44</sup>Roane State Community College, Oak Ridge, TN 37830, USA. <sup>45</sup>Université Côte d’Azur, Observatoire de la Côte d’Azur, Laboratoire Lagrange/ Centre National de la Recherche Scientifique, Unité Mixte de Recherche 7293, 06304 Nice Cedex 4, France. <sup>46</sup>Institute for Astronomy, University of Hawaii, Honolulu, HI 96822, USA.

\*Corresponding author. Email: spencer@boulder.swri.edu

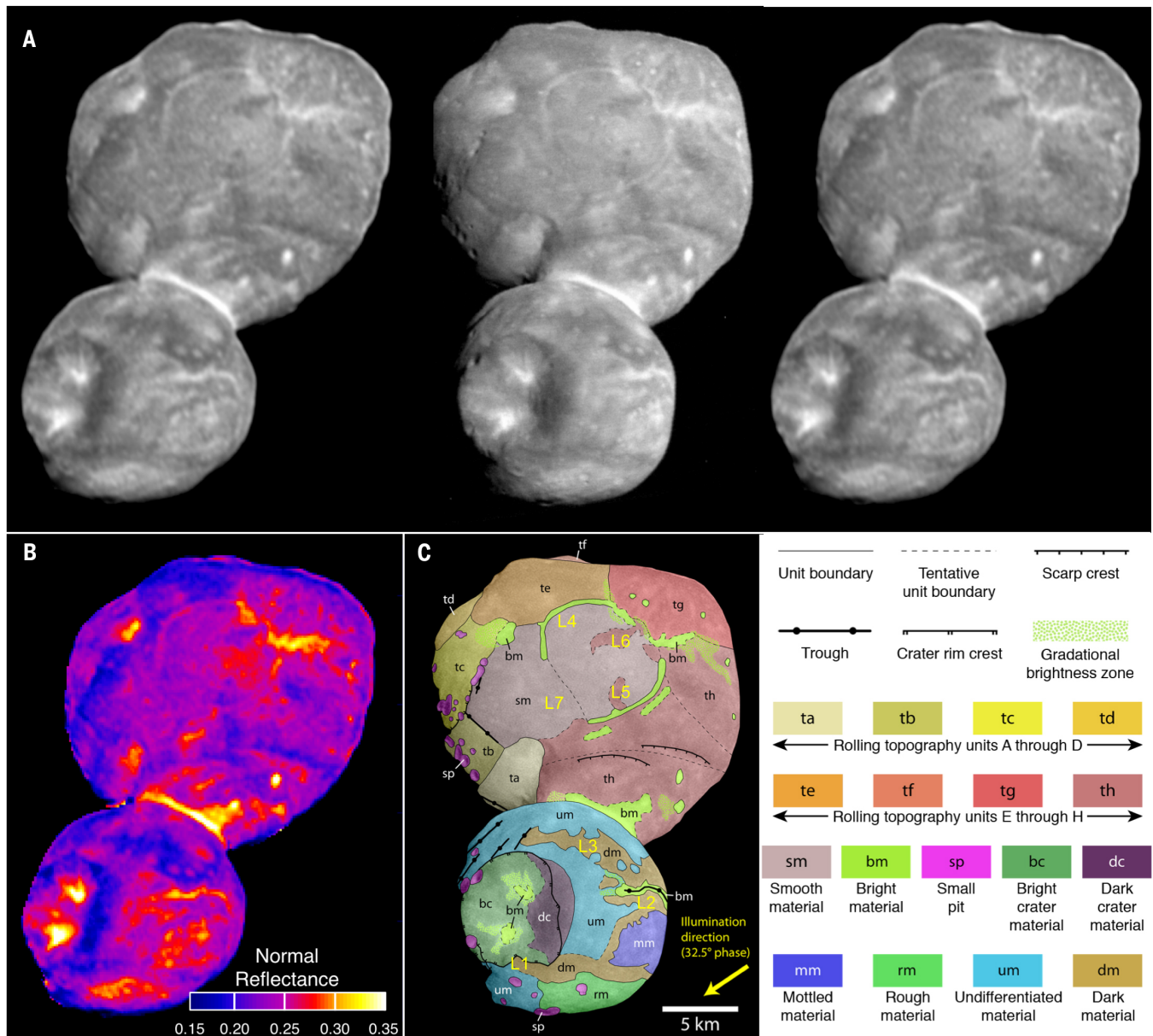


**Fig. 1. Mapping of Arrokoth.** (A) Cross-eyed (left+center) and direct (center+right) stereo pair image of Arrokoth, taken by LORRI. The left and right images are CA04, range = 27,850 km, phase = 12.9°, 138 m pixel<sup>-1</sup>; the center image is CA06, range = 6634 km, phase = 32.5°, 33 m pixel<sup>-1</sup>. Both images have been deconvolved to remove the LORRI point-spread function, and motion blur from CA06, to maximize detail (9). (B) A 0.6- $\mu$ m normal reflectance map of Arrokoth, based on image CA04. (C) Geomorphological map of Arrokoth, overlain on the deconvolved CA06 image. The positive spin axis of Arrokoth is pointing approximately into the page. Yellow labels L1 to L7 identify locations mentioned in the text. Geological units are labeled and colored as shown in the legend.

smaller than the 200-m vertical resolution of the terrain model. Our interpretation is based on both the terrain model and subjective analysis of the stereo pair.

#### Rotation and global shape modeling

No periodic brightness variation due to rotation was detected in Hubble Space Telescope (HST) photometry before the flyby, with an upper limit amplitude of about 0.15 magnitudes (10). Stellar occultations in July 2017 and August 2018 showed that Arrokoth had an elongated, possibly contact-binary shape

(11). The elongated shape and the low light-curve amplitude implied that Arrokoth's rotational pole was roughly aligned with the direction of the Sun and Earth.

Arrokoth's rotation and global shape are mostly determined from LORRI images taken between 2.2 days before the encounter, when Arrokoth first exceeded 2 pixels in length, and 9 min after encounter, when Arrokoth was last imaged (at high phase angle) as a receding crescent (Fig. 3). Disk-integrated photometry from earlier unresolved LORRI images showed no periodic variations in brightness, with an

upper limit amplitude of 0.1 magnitudes (12), but were affected by confusion from the dense stellar background. The strongest constraints on the shape model are from a series of approach images with a cadence between 1 hour and 20 min, starting 13.6 hours before closest approach, when Arrokoth subtended 10 pixels in length (Fig. 4A). These images covered 85% of the 15.92-hour rotation period, though only one hemisphere of Arrokoth was visible because of the near-alignment of the rotational pole with both the direction of the Sun and New Horizons' approach direction.

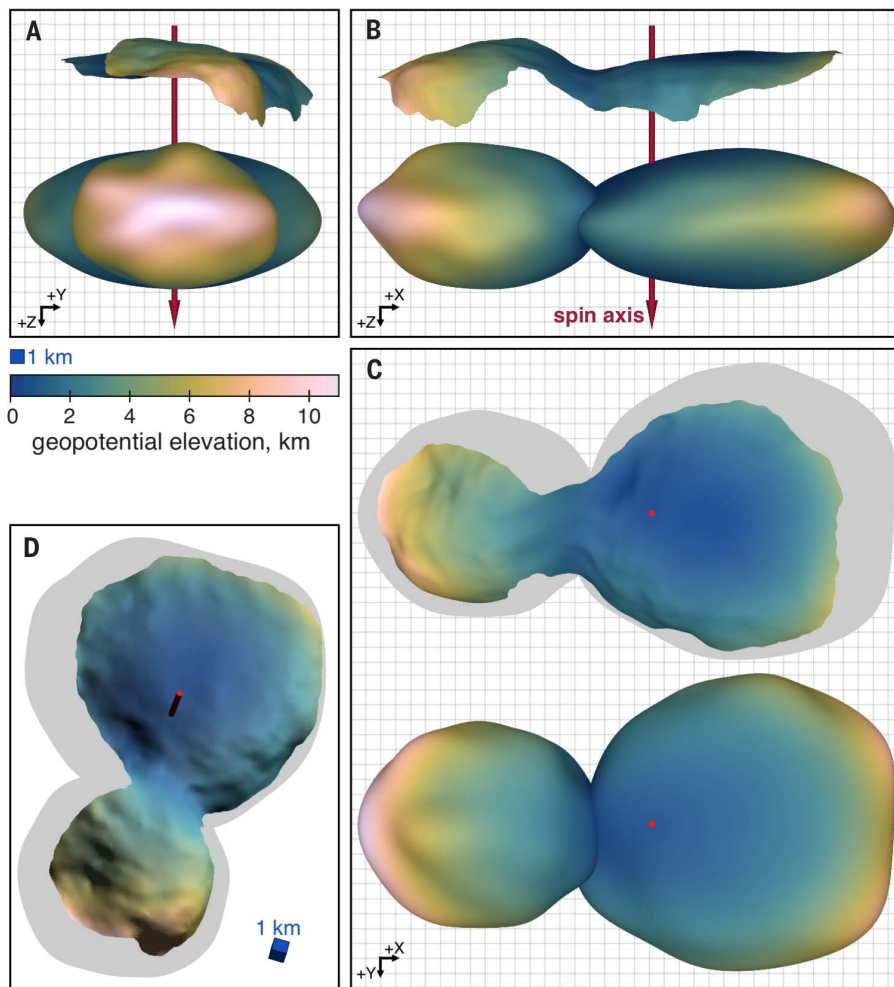


**Fig. 2. Stereo and global shape models.** (A to C) Comparison of the stereo shape model of the encounter face (top of each panel) to the global shape model (bottom of each panel), as seen from the  $-X$  (small lobe) direction (A), the  $+Y$  direction (B), and the south polar ( $-Z$ ) direction (C). The red arrow shows the orientation and location of the positive spin axis. Each model is colored to show the variation in geopotential across the surface. The stereo model has been trimmed to remove edge effects. (D) Stereo model seen from the same geometry as the CA06 observation (Fig. 1A, center), but with different lighting, chosen to highlight the small-scale topography.

Incorporating the additional rotational coverage images now available into the same rotational modeling techniques as before (1), the rotational period of Arrokoth is unchanged at  $15.92 \pm 0.02$  hours, but its pole orientation has been refined. The positive rotational pole points to right ascension  $317.5 \pm 1^\circ$ , declination  $-24.9 \pm 1^\circ$  in the J2000 equinox. The rotation rate is within the range of other CCKBOs (13–15). The resulting obliquity of Arrokoth's pole to its orbit is  $99 \pm 1^\circ$ , and the rotational pole is  $39 \pm 1^\circ$  from the New Horizons approach vector and  $28 \pm 1^\circ$  from the direction from the Sun to Arrokoth during the encounter. The rotational brightness variation implied by the shape model would have a peak-to-peak amplitude of 0.05 magnitudes from New Horizons' approach direction, consistent with the earlier nondetections.

A low-resolution global shape model [data S2 and Movie 1 (9)] was produced using all available observations—including the early, distant ones—to refine the model. The high phase angle CA07 observation [Fig. 3 and table S1 (9)], of the illuminated double crescent of Arrokoth, provides a constraint on how thick the unilluminated side can be, based on which stars are and are not eclipsed by the object (Fig. 4B). There remain differences between the shape model and the LORRI images in Fig. 4A; e.g., compared to the model, the images show a less indented neck and flatter outer end of the small lobe between December 31 20:38 and January 1 01:12.

The best-fitting global shape model consists of two roughly ellipsoidal lobes with overall dimensions X, Y, and Z of 36 km by 20 km by 10 km. Maximum dimensions of the large and small lobes are 20.6 km by 19.9 km by

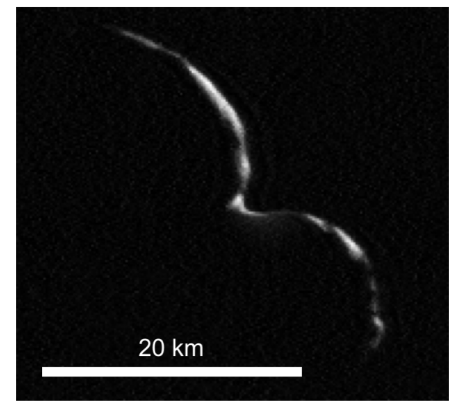


**Fig. 3. Arrokoth seen at high phase.** New Horizons' last view of Arrokoth (CA07), taken with the LORRI camera 9.4 min after closest approach at phase angle  $152.4^\circ$ , range 8834 km, and resolution  $175 \text{ m pixel}^{-1}$ . This image has been deconvolved to remove the motion smear visible in Fig. 4B (9). The large lobe is in the upper left and the small lobe is in the lower right.

9.4 km and 15.4 km by 13.8 km by 9.8 km, respectively. The uncertainty for these dimensions is roughly 0.5 km by 0.5 km by 2.0 km in X, Y, and Z, respectively; it is larger in the Z direction because the flyby imaged little of the  $+Z$  (northern) half of the object. The total volume is  $3210 \pm 650 \text{ km}^3$ , equivalent to a sphere of diameter  $18.3 \pm 1.2 \text{ km}$ . This volume is 30% larger than the previous estimate of  $2450 \pm 720 \text{ km}^3$  (1), though consistent within the uncertainties. The larger lobe has a volume equal to a sphere of diameter  $15.9 \pm 1.0 \text{ km}$ , whereas the equivalent diameter for the smaller lobe is  $12.9 \pm 0.8 \text{ km}$ . These values lead to a volume ratio (and mass ratio if densities are equal) of  $1.9 \pm 0.5$ .

Figure 2 compares the global shape model to the stereo model of the encounter ( $-Z$ ) side of Arrokoth. There is broad agreement between the two techniques, although the south polar region of the large lobe is flatter in the stereo model, and the neck is smoother (a slope discontinuity at the neck is an intrinsic feature of the global shape model, owing to its dual-lobe nature). We regard the stereo model as more reliable than the global shape model in the south polar and neck regions, because the stereo model incorporates additional information due to the matching of albedo features and because these albedo features can also produce artifacts in the global shape model, which assumes a uniform surface albedo. However, near the limbs, the stereo model performs poorly because foreshortening makes feature matching difficult, whereas the global shape model is well constrained near the limbs.

### Gravity modeling

The irregular shape of Arrokoth produces a complex geophysical environment. We calculated

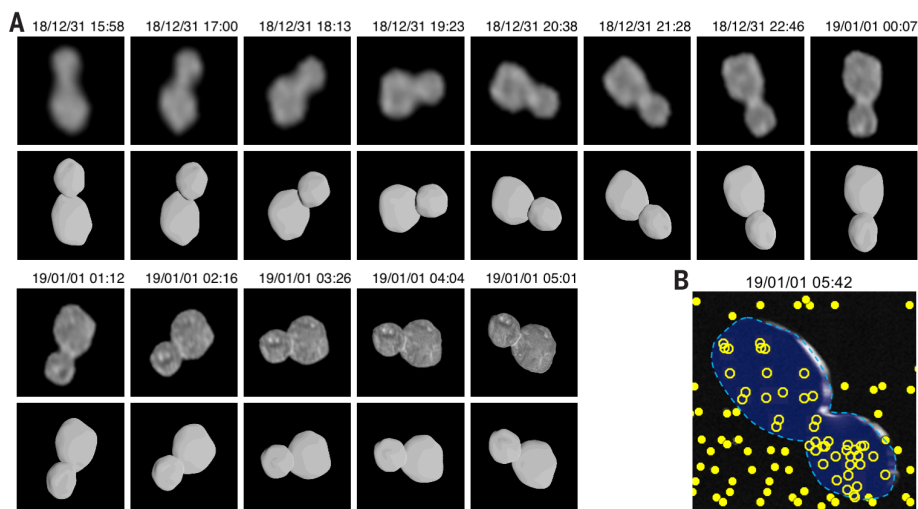
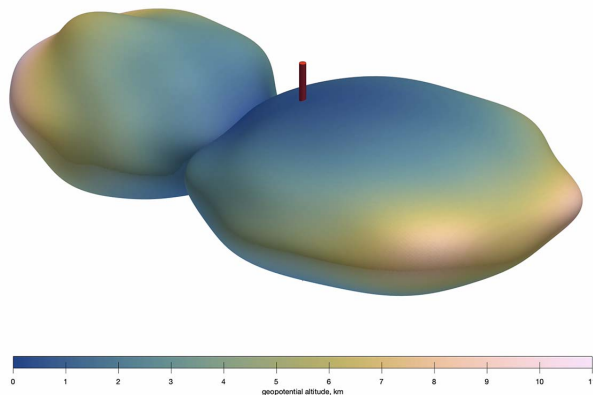


**Fig. 4. Shape model compared to LORRI images.** (A) Deconvolved LORRI approach images of Arrokoth, compared to synthetic images with the same geometry derived from the global shape model. Images have been scaled to a constant frame size of 44 km by 44 km, so become sharper as time progresses and range decreases. Celestial north is up. (B) The CA07 departure image, with the silhouette (dark blue) and outline (light blue dashed line) of the shape model superposed. Open and filled yellow dots indicate the locations of occulted and unocculted stars, respectively, in the six-frame CA07 sequence, used to constrain the shape of the unilluminated hemisphere.



**Movie 1. Animation of the global shape model of Arrokoth.** The model is shown rotating about its true spin axis (red arrow), highlighting the encounter hemisphere. The model is colored to show geopotential altitude and is obliquely illuminated.

Arrokoth's geopotential (the sum of the gravitational and rotational potentials in a body-fixed reference frame) using the low-resolution global shape model, the 15.92-hour rotation period, and an assumed bulk density. In the absence of spacecraft gravity measurements or detected satellites, the density of Arrokoth is not directly constrained. However, if the neck of Arrokoth is assumed to have no tensile strength, the density must be  $>290 \text{ kg m}^{-3}$ , or the rotation would overcome the mutual gravity of the two lobes, causing them to separate. We assume a nominal bulk density of  $500 \text{ kg m}^{-3}$ , similar to the measured densities of cometary nuclei [e.g., comet 67P/Churyumov-

Gerasimenko (16)], which leads to a mean surface gravity of  $\sim 1 \text{ mm s}^{-2}$ . If this density is correct, the requirement for the two lobes to support each other against their mutual gravity over their  $\sim 28 \text{ km}^2$  contact area implies a compressive strength (accounting for centrifugal force) of  $>2.3 \text{ kPa}$ .

Figure 2 uses color to show the geopotential altitude, calculated by dividing the geopotential by the total acceleration, which represents elevation with respect to a gravitational equipotential surface (17). The geopotential is calculated from the global shape model, then evaluated on the surfaces of the global shape model and the stereo model [with positions

matched to the global shape model (9)]. This approach results in slight inaccuracies in the geopotential calculated across the stereo model, as there are regions where the stereo model rises above or below the surface of the global shape model. We focus on general trends that are robust to the uncertainties in the shape model. The geopotential is highest at the distal ends and equator and decreases with increasing latitude on each lobe, reaching a global minimum at the neck. For an assumed density of  $500 \text{ kg m}^{-3}$ , surface slopes [derivatives of the geopotential (17)] are generally gentle ( $<20^\circ$ ) and slope downward to higher latitudes and into the neck region (fig. S1). If material can flow downslope, then it will collect at higher latitudes and in the neck region. The stereo model shows that the neck is relatively smooth compared to its sharp appearance in the global shape model, with shallow slopes. The global shape model shows slopes of  $>30^\circ$  at the neck, but this steepness is in part an artifact of the global model's treatment of Arrokoth as two separate overlapping bodies.

The configuration of the two lobes of Arrokoth has implications for its formation and evolution (1, 18). Using the same assumptions as above, we calculate the principal axes of inertia for the two lobes by dividing the model at the narrowest point of the neck. This confirms that the large lobe's highest moment of inertia axis is aligned within  $<5^\circ$  of its small lobe counterpart, and the equatorial planes of the two bodies are also almost coincident in space, with the estimated center of mass of the small lobe displaced only 0.2 km from the equatorial plane of the large lobe.

### Surface units

Figure 1B shows a map of  $0.6\text{-}\mu\text{m}$  normal reflectance (19). The map is derived from the high-SNR CA04 image, using a merger of the global and stereo shape models to determine illumination at each point, and an assumed lunar-like photometric function, which has no limb darkening at zero phase (20). The normal reflectance is equal to the geometric albedo of a body covered in material with that location's photometric properties. Arrokoth's mean  $0.6\text{-}\mu\text{m}$  normal reflectance, and thus its geometric albedo, is 0.23. The mean and standard deviation of the normal reflectance are 0.230 and 0.035, respectively, for the large lobe, and 0.228 and 0.043, respectively, for the small lobe.

We have also produced (9) an updated geological unit map of Arrokoth (Fig. 1C) that supersedes the previous preliminary map (1). This mapping is physiographic in nature and is not intended to rigorously convey stratigraphic relations between units. The small and large lobes have distinctly different surface appearances, so we mapped their surface units separately and describe them separately below.

### Small lobe

This lobe is dominated by a large depression (informally named Maryland), which is very likely to be an impact crater (*I*). The projected crater rim measures ~6.7 km by 6 km across in the image plane, with its longer axis roughly aligned with the principal axis of Arrokoth. The ellipticity might be due to foreshortening, in which case Maryland could be circular with a diameter of 6.7 km. Stereo measurements show that the deepest well-determined point in Maryland is 0.51 km below a plane defined by the rim, or 1.3 km below the surface of a sphere with the small lobe's mean radius, giving a depth/diameter ratio of 0.08 to 0.19. This depth/diameter ratio is similar to that of craters on other bodies with gravities similar to Arrokoth's  $\sim 1 \text{ mm s}^{-2}$ , including asteroids Šteins [ $\sim 0.12, 0.8$  to  $1.3 \text{ mm s}^{-2}$  (*21*)] and Eros [ $\sim 0.13, 2.4$  to  $5.5 \text{ mm s}^{-2}$  (*22*)], though these bodies are composed of different materials and may have different porosities. Stereo imaging (Fig. 1A) reveals that the part of its rim furthest from the large lobe features a promontory protruding into the crater (marked L1 in Fig. 1C), at an elevation similar to the rest of the rim, which is not a common feature of impact crater rims.

Albedo patterns across the small lobe are complex. There are two patches of bright material (unit bm) within Maryland, which show discrete boundaries near the crater bottom, and fade toward the crater rim. Straddling the Maryland rim on the side opposite the bright patches is discrete, dark crater rim material (unit dc), which contrasts with the brighter terrain (unit bc) that forms the remainder of the crater interior. Elsewhere on the small lobe, discrete morphological units have albedo variations of almost a factor of 2 (Fig. 1B). The rough terrain at the distal end of the small lobe (unit rm) forms a facet that is relatively flat compared to the overall curvature of the surface and is brighter than its immediate surroundings. The low illumination angle on this facet reveals a rough surface texture at a scale of a few hundred meters, apparently mostly composed of sub-kilometer pits, with one prominent ~340-m-diameter pit (marked 27 in Fig. 6A) that resembles a small, fresh, bowl-shaped impact crater. Another nearby mottled bright unit (mm) may be similar, but it is seen at a higher illumination angle so topographic roughness is not apparent, and it has a distinctly crenulated and angular margin relative to that of unit rm (L2 in Fig. 1C).

Dark material surrounding the mm unit seems to be part of a discrete unit, designated *dm*, that wraps around much of the remainder of the observable surface of the small lobe—this material is the darkest on Arrokoth, with minimum 0.6- $\mu\text{m}$  reflectance of 0.18. In places (L3 in Fig. 1C), it has a boundary with pointed

and angular protrusions and rounded indentations, which may indicate material erosion and removal due to scarp retreat (*I*). Near L3 in Fig. 1C, there are also bright circular patches within the dark material. Running down the center of the principal mapped outcrop of dark material is a sinuous unit of bright material (unit bm), which stereo observations show

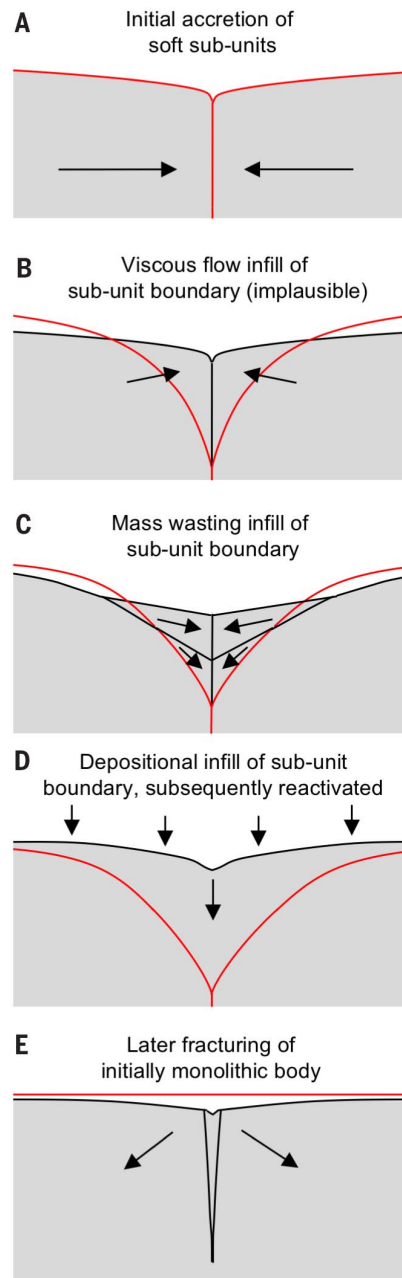


**Fig. 5. Possible explanations for the appearance of the boundaries between terrain subunits on the large lobe.** The original surface (shown in red) is modified by the processes labeled in each panel. We consider options (D) and (E) to be most consistent with the available evidence; see text for discussion.

occupies a V-shaped trough. The rest of the surface of the small lobe is nondescript at the available lighting and resolution and has been mapped as undifferentiated material (unit um). Crossing the undifferentiated material near the terminator between Maryland and the large lobe are a series of roughly parallel troughs, which are reminiscent of structural troughs seen on other similar-sized bodies—for instance, asteroid Eros (*23, 24*), Saturn satellites Epimetheus and Pandora (*25*), and the Martian satellite Phobos (*26*).

Our data confirm that the bright neck region connecting the two lobes has a diffuse margin at least on the large lobe side, but extreme foreshortening makes it difficult to characterize its margin on the small lobe side.

### Large lobe

The larger lobe is very different in appearance from the small lobe. Previous analysis (*I*) mapped the large lobe as composed of a series of roughly equal-sized, discretely bounded, rolling topographic units. We interpret some of these units and their boundaries differently, though confirm the discrete nature of many of the units (ta through tg). Those near the terminator, ta–td, are distinctive, being brighter than adjacent units (Fig. 1B) [though ta is noticeably less red than the others (*3*)], and are clearly separated from the rest of the large lobe by a common, continuous scarp or trough and chain of pits. Units tg and th appear more mottled than adjacent units, and stereo imaging of these suggests that their surface consists of dark ridges and hills surrounded by brighter low terrain.

The rest of the large lobe is occupied by smooth material (unit sm) of moderate albedo, transected by a series of distinctive bright linear features (unit bm), some of which form an incomplete annulus. In some areas (e.g., L4 in Fig. 1C), the inner margin of the annulus appears sharply bounded, possibly with an outward-facing scarp, whereas the outer margin is more diffuse. Stereo observations (Figs. 1A and 2D) show that terrain within the annulus is flatter than the undulating surface of the rest of the visible portion of the large lobe and suggest that the annulus occupies a shallow trough. At the boundary between units tg and sm, the annulus appears to be interrupted by diffuse bright material, which may be superimposed upon it. In two places, L5 and L6 in Fig. 1C, dark hills appear to extend into the sm unit. At L5 in Fig. 1C, these hills seem to be an extension, cut by the bm annulus, of similar hills on unit th. We discuss the possible origin of these features below.

### Geological interpretation

Our data, particularly the stereo images, confirm that the brighter material on both lobes occurs preferentially in depressions. The

brightest material on the large lobe (the possible crater numbered 17 in Fig. 6A), on the small lobe (bright features 42 and 43 in Fig. 6A), and in the bright collar between the two lobes all have normal  $0.6\text{-}\mu\text{m}$  reflectance values near 0.37, suggesting that the bright material has similar chemical and physical properties in all these regions. The most extensive bright region, the bright collar in the topographic low of the neck region, may be simply the largest-scale example of a general process that creates bright low-lying material across Arrokoth. As previously proposed (1), loose, poorly consolidated, likely fine-grained bright material may move downslope and accumulate in depressions, which would imply that bright material is more mobile than dark material on Arrokoth. The complex albedo patterns on the small lobe, and their crenulated margins, may result from the exposure and differential erosion of multiple lighter and darker layers oriented roughly parallel to its surface, though independent topographic information is of insufficient quality to confirm this explanation.

It was previously proposed (1) that the large lobe might be composed of smaller subunits that accreted separately. However, the improved imagery and topography raise issues with this interpretation. First, the central bm annulus, enclosing what was mapped as a discrete subunit in (1), appears to be younger than some other surface features, and not an unmodified primordial boundary, for the following reasons: (i) The annulus is incomplete, with no discernable topographic feature or textural change in the gap region where it is missing (L7 in Fig. 1C)—for this reason we map a continuous unit, sm, across this gap; (ii) even where the annulus is conspicuous, it cuts across flat terrain for most of its length; and (iii) dark hills found on the th and sm subunits appear to form a continuous physiographic unit cut by the annulus (at L5 in Fig. 1C), and (iv) the partially concentric nature of the annulus suggests a structural basis, not greatly obscured by subsequent deposition. Second, though other proposed subunits are distinguishable by differing surface textures, albedos, and modest topographic inflections or other surface features, the overall shape of the large lobe is smooth and undulating. There are no major topographic discontinuities between the subunits comparable to that between the two lobes, as would be expected if the subunits had a similar internal strength to the lobes as a whole. Erosion and alteration over the past 4.5 billion years (Ga) (see below) are likely to have modified the optical surface and the uppermost few meters (27) but probably do not explain the smoothness seen at the  $>30\text{-m}$  scale of the New Horizons imaging resolution.

Some possible explanations for the appearance of the annulus and other subunit bound-

aries are illustrated in Fig. 5. The subunits may have been soft enough at the time of merger that they conformed to each other's shapes on contact (1, 28, 29) (Fig. 5A), though no evidence for impact deformation is seen. For such deformation to take place at the time, the shear strength of the merging components must have been no more than 2 kPa, the ram pressure of an impacting body assuming a merger velocity of 1 to 2  $\text{m s}^{-1}$  and a material density of  $500 \text{ kg m}^{-3}$ . The possibility that subunits flowed viscously as a result of gravity after contact while still soft (Fig. 5B) can be discounted, because such flow would require an implausibly low shear strength of  $\sim 100 \text{ Pa}$ . Erosion and downslope movement (mass wasting) may have filled in original gaps between the subunits (Fig. 5C), though there is an absence of obvious boundaries (except perhaps at the tg/sm contact) between material transported by mass wasting and in situ material.

The fact that mass wasting has not filled the much larger depression between the two lobes also implies that any major mass wasting process must have ceased before the merger of the two lobes. The original discontinuities may have been buried by subsequent accretion or redistribution of surface material (Fig. 5D). The boundaries would then need to be re-activated in some way to still be visible on the surface, possibly by collapse into subsurface voids or degassing of volatiles such as  $\text{N}_2$  or  $\text{CO}$ , which may explain the trough-like appearance of parts of the bm annulus, and the troughs and pit chains seen at low illumination angle between the ta - td subunits and the rest of the larger lobe. However, it's not clear how burial could preserve different surface textures for the different subunits. Alternatively, the large lobe may be monolithic, and the visible boundaries may be secondary features (Fig. 5E), e.g., produced by subsequent

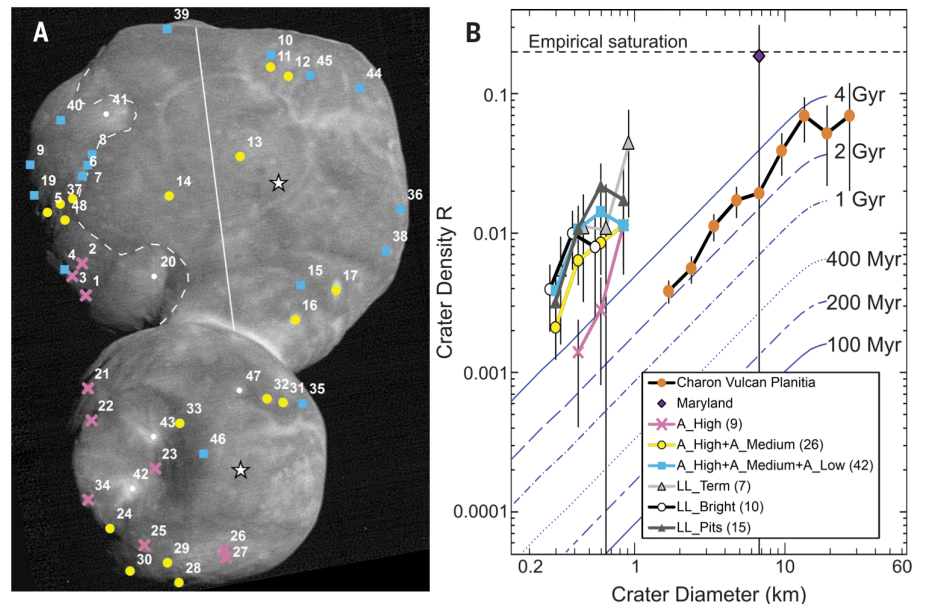


**Fig. 6. Craters and Pits on Arrokoth.** (A) Locations of features considered for crater analysis; numbers refer to crater listings in data S3. Color denotes confidence class: pink, high confidence (A\_High); yellow, medium confidence (A\_Medium); light blue, low confidence (A\_Low). Features indicated in white are considered to be highly unlikely to be of impact origin and are not included in the crater statistics. The solid white line splits the large lobe into regions with differing lighting conditions, a more obliquely illuminated region with more visible depressions (LL\_Pits, left) and a more vertically illuminated region with bright spots (LL\_Bright, right). The white dashed curve delineates the boundary of combined geologic units ta, td, tc, and td (LL\_Term), considered together for crater density determination. The star symbols indicate the planetocentric subsolar point on each lobe according to the shape model. Lighting direction is shown in Fig. 1C. (B) The size-frequency distribution of craters on Arrokoth for each crater subgroup and region described in the text and shown in (A) and (9). The yellow curve includes both high- and medium-confidence classes, and the light blue curve includes all confidence classes. Parenthetical numbers are the total number of craters and pits in each category. The Arrokoth crater data are compared to crater densities on Charon's Vulcan Planitia (39) without diameter adjustments for gravity or velocity scaling, and to predictions based on an impactor flux model for six different ages of surfaces on Arrokoth and gravity regime scaling [blue curves with different line styles (5)]. The LL\_Term and LL\_Bright distributions are offset horizontally by  $\pm 9\%$  for clarity. The empirical saturation line refers to a  $D^{-3}$  differential power law distribution (72). Myr, million year; Gyr, billion year.

fracturing. For the annulus, we consider the evidence to be most consistent with scenarios D and E in Fig. 5. However, in any of these cases, the processes that produced the distinctive surface textural contrasts between the units, in particular the patches of dark hills and ridges, are unknown.

### Pits and craters

In addition to the 7-km-diameter probable impact crater Maryland, scattered across the body of Arrokoth are numerous roughly circular subkilometer bright patches and pits, though even if these are mostly impact craters, the crater density is relatively low compared to many other small bodies (*J*) (fig. S2). The bright patches are generally seen in areas that have high illumination angle and are away from the terminator. Some of these patches appear in stereo imaging (Fig. 1A) to occupy depressions. These may be equivalent to the pits seen in low-illumination angle areas near the terminator (unit sp, Fig. 1C): These pits might also feature bright material on their floors that is invisible because of the unfavorable lighting.

We have classified these bright patches and pits to reflect our confidence that they are impact craters, based on the morphology expected for either fresh or degraded impact craters (9) (supplementary text), as determined by multiple independent investigators. Crater candidates and their classifications are listed in data S3 and shown in Fig. 6A. Our criteria included the spatial arrangement of the potential craters and their relationship to other geologic features. For instance, as noted above, a chain of pits that is coincident with a scarp on the boundary between units tc and sm possibly originated through surface collapse rather than impact (*T*). For a fresh crater formed on a flat and smooth surface, a crater rim is expected to be close to circular and raised above the surrounding terrain [unless the terrain is substantially porous (30)], though image resolution does not always allow identification of a raised rim. The interior shape of a crater is expected to be bowl-like with a depth/diameter ratio typically not higher than  $\sim 0.2$  (31). The predicted modal impact velocity onto Arrokoth is  $\sim 300 \text{ m s}^{-1}$  (5), which is sufficient to form craters with typical morphologies (see supplementary text). In the case of Arrokoth, the lowest-velocity impacts ( $\leq 20 \text{ m s}^{-1}$ ) are unlikely to leave conspicuous depressions, but these impacts are expected to be a small fraction of the total (5). The formation of a crater on a slope or modification by later geologic processes (such as mass wasting or a subsequent fault near the crater) may also alter the crater's appearance.

Potential small craters were subdivided in three ways (Fig. 6A) (9): (i) All pits and bright patches were subdivided based on our confi-

dence that they are impact craters; (ii) features on the large lobe were subdivided into pits nearer the terminator, and bright patches away from the terminator, as shown in Fig. 6A; and (iii) a combination of geologic units—ta, tb, tc, and td, designated “LL\_Term” as they are on the large lobe terminator (Fig. 6A)—was analyzed separately, because the entire combined unit has low-angle lighting optimal for crater identification. These subdivisions yielded a range of plausible crater densities, shown in Fig. 6B as a crater relative- or R plot (9). Overall R values for each dataset are somewhat uncertain as they depend on the areas used for each distribution, and densities are lower if uncertain craters are excluded. The resulting uncertainty range of crater densities is less than a factor of 10 in each diameter bin in Fig. 6B.

Besides Maryland, all other possible impact features are 1 km in diameter or smaller. Although the diameter gap between Maryland and second-largest crater on Arrokoth is large, the gap does not strongly disfavor a single power-law size distribution for the craters. We tested a model crater population with a power-law size distribution with slope  $q = -2$  against the observed Arrokoth craters in the combined “A\_High” and “A\_Medium” categories. The resulting Anderson-Darling statistic indicates no substantial disagreement between the model and observed sample, with a significance level of  $p \leq 17\%$ .

Our analysis shows that Arrokoth appears to be only modestly cratered, relative to heavily cratered small objects like Phobos (fig. S2), and there are some areas on Arrokoth where very few, if any, potential craters exist, in particular the part of the large lobe between the dashed and solid white lines in Fig. 6A.

The age of the surface can be estimated from the observed crater density. We converted impact flux estimates for Arrokoth to crater densities corresponding to several surface ages (5) and show these in Fig. 6B. The resulting age estimates are uncertain, given the uncertainty in identifying which craters are impact generated, and because the model curves shift on the basis of the crater scaling parameters used. Scaling in the strength regime, as opposed to scaling in the gravity regime assumed here (5), could in principle reduce the sizes of craters produced, if the surface strength of Arrokoth were sufficiently high. The expected strengths of porous cometary surfaces are, however, generally low enough [ $\sim 1 \text{ kPa}$  or less (32)] that the observed craters on Arrokoth should have formed in the gravity regime. By contrast, accounting for the additional cratering in an early but brief dynamical instability phase in the outer Solar System (33) would shift the model curves in Fig. 6B upward, although possibly by no more than a factor of 2 (5). Low relative densities of small craters are also ob-

served on near-Earth asteroids and are conventionally explained as being due to seismic shaking from larger impacts or surface evolution due to changes in spin state (34–36). However, Arrokoth's spin state is likely to have evolved only very slowly (18), there do not appear to be sufficient impacts to act as effective seismic sources, and Arrokoth's likely high porosity would make seismic energy propagation highly inefficient. Overall, despite the paucity of craters on its surface, the observed crater density is consistent with a crater retention age of greater than  $\sim 4$  billion years. The visible surface at the scale of the LORRI image resolution thus plausibly dates from the end of Solar System accretion.

Though the diameters of observed craters on Arrokoth (apart from Maryland) are smaller than those measured in the Pluto system, the slopes of the Arrokoth and Pluto system craters are consistent given the small number statistics. Using approximate Bayesian computation forward-modeling methods (37, 38), we estimated the posterior probability density functions for the parameters of independent truncated power-law crater size–frequency distribution models for Arrokoth's and Charon's (39) observed crater populations (for craters  $< 10 \text{ km}$  in diameter, below the break in slope observed on Charon). We then conducted the same analysis for a model with a common slope,  $q$ , between the two populations, but a separate offset. The mean slope  $q = -1.8_{-0.6}^{+0.4}$  for Charon alone,  $q = -2.3_{-0.6}^{+0.6}$  for Arrokoth alone, and  $q = -2.0_{-0.3}^{+0.4}$  for the joint set (95% confidence). However, as seen in Fig. 6B, crater density on Arrokoth is higher than would be obtained from an extrapolation of the Charon slope and density to subkilometer craters.

### Satellites and rings

Before the Arrokoth flyby, constraints on the prevalence of satellites and rings around sub-100-km-diameter Kuiper Belt objects were limited. Larger CCKBOs are frequently members of orbiting binary pairs (40). Satellites with a primary/secondary brightness ratio larger than 20 have not been found for KBOs smaller than 500 km in diameter (41), though this is likely in part due to observational biases. By contrast, satellites with high primary/secondary brightness ratio are common around large KBOs in non-CCKBO populations. The presence or absence of satellites provides a constraint on formation of the Arrokoth contact binary (e.g., a satellite could potentially remove angular momentum from the central body). At least two known asteroid contact binaries have small satellites: The large Trojan asteroid Hektor has a satellite that orbits at only 5 times the primary radius and has a diameter of 5% of the primary (42), and the large bilobed main-belt asteroid Kleopatra has two known satellites orbiting at 8 and 12 times the primary

radius, with diameters 6% that of the primary (43).

New Horizons conducted a nested series of satellite searches with the LORRI camera during its approach to Arrokoth, using stacks of many images taken using 4 by 4 pixel binning to increase sensitivity and reduce data volume. Our dataset allows a deeper and broader search than previously reported (1, 9). No satellites have been found. We can exclude satellites larger than 100 to 180 m in diameter (~0.5% the diameter of the primary) on orbits ranging from Arrokoth's surface to 8000-km radius, and <300 m in diameter throughout most of the Hill sphere (the region within which a moon could be gravitationally bound to Arrokoth), assuming albedos similar to that of Arrokoth itself (Fig. 7). Satellites analogous to those of Hektor and Kleopatra can thus be excluded.

The prevalence of rings around small KBOs is poorly constrained, but they are known to exist around Chariklo (44), Haumea (45), and perhaps Chiron (46). We searched for rings and dust clouds within the Arrokoth environment at all phases of the encounter. The LORRI satellite searches on approach, discussed above, constrained backscattered light due to any ring or dust clouds to  $I/F \leq 2 \times 10^{-7}$  (19) at  $11^\circ$  phase for a 10-km-wide ring, assuming neutral colors (1). This limit is fainter than Jupiter's main ring [ $I/F = 7 \times 10^{-7}$  at  $11^\circ$  phase (47)]. We also conducted dedicated ring searches in forward-scattered light after closest approach, using images taken 1.7 to 2.3 hours after closest approach at a phase angle of  $168^\circ$ , covering radii up to 6000 km from Arrokoth. The MVIC instrument, which has better rejection of scattered sunlight than LORRI, was used in its panchromatic framing mode, with total

exposure times of 30 s. Reduction and analysis followed methodologies used for similar Pluto data (48). No rings or dust structures were detected, with an upper limit  $I/F$  of  $\sim 1.5 \times 10^{-6}$  for structures wider than about 10 km in Arrokoth's equatorial plane (fig. S4). Any ring around Arrokoth is thus also fainter in forward scattering than Jupiter's main ring [ $I/F = 4 \times 10^{-6}$  at this phase angle (47)].

New Horizons' Student Dust Detector (SDC) instrument (49) detected no signals above the noise threshold within  $\pm 5$  days of the Arrokoth encounter, implying that there were no impacts by dust particles  $>1.6 \mu\text{m}$  in radius, giving a 90% confidence upper limit of  $3 \times 10^7$  particles  $\text{km}^{-2}$ . For 10% albedo, this is equivalent to an  $I/F$  limit of  $3 \times 10^{-11}$ , even more constraining than the optical limit, for particles of this size or larger along the spacecraft trajectory.

### Comparison to other KBOs, and to possible captured KBOs

Though most other known CCKBOs are larger than Arrokoth, owing to observational biases, Arrokoth appears typical of CCKBOs using the few metrics that can be directly compared. Arrokoth's 0.6- $\mu\text{m}$  geometric albedo, 0.23, is within the known range of other CCKBOs (50). Rotational lightcurves suggest that up to 25% of larger CCKBOs could be contact binaries like Arrokoth (13), though contact binaries appear to be more abundant, up to 50%, in the Plutino population (51). Arrokoth's color is also typical of CCKBOs (1, 3).

Many irregular satellites of the giant planets may be captured KBOs, but only three have resolved spacecraft images. Neptune's satellite Triton, with a diameter of 2700 km, is far too large and active to be a useful comparison

body to Arrokoth. Neptune's smaller irregular satellite Nereid, 170 km in diameter, has a geometric albedo of 0.16 to 0.20, similar to Arrokoth's, but is neutral in color (52). Saturn's 210-km-diameter irregular satellite Phoebe [possibly a captured Kuiper Belt object (53), though perhaps instead a captured C-type asteroid (54, 55)], is darker [geometric albedo 0.08 (56)] and less red (57), and has a completely different surface appearance, dominated entirely by impact features (58). If Phoebe ever resembled Arrokoth, it has been drastically altered by subsequent evolution.

### Comparison to Jupiter family comets

A class of objects previously explored by spacecraft that may be analogous to Arrokoth in ultimate origin are the Jupiter family comets (JFCs). These differ from Arrokoth in three major respects: (i) Provenance: The vast majority of these bodies likely originated in the Kuiper belt, but from a different family of KBOs: the population of "scattered KBOs," which likely originated closer to the Sun than Arrokoth, and whose orbits are strongly perturbed by gravitational interactions with Neptune (59). (ii) Size: The effective spherical diameters of the JFC nuclei visited by spacecraft are 3 to 18 times smaller than that of Arrokoth. (iii) Thermal history: JFCs have experienced intense solar heating, which has heavily modified their surfaces. By comparing the properties of Arrokoth and JFC nuclei, we can explore the effects of these differences.

The JFC nuclei visited by spacecraft have diverse shapes and surfaces (Fig. 8, fig. S3, and table S3). Comets 19P, 67P, and 103P appear to be highly elongated bilobate objects, suggesting the merger of two distinct bodies, as has been proposed for Arrokoth (1, 18), though for comets it is also possible that thermal evolution has generated this shape [e.g., (60)]. Except for 67P, whose bulk density is  $538 \pm 1 \text{ kg m}^{-3}$  (16), the densities of the other JFC nuclei are uncertain by a factor of 2 or more, but all are consistent with  $\sim 500 \text{ kg m}^{-3}$  (61), which implies average bulk porosities of  $\sim 50$  to  $80\%$ . Arrokoth's density is likely greater than  $290 \text{ kg m}^{-3}$  (see above), and thus at least consistent with those of JFC nuclei. The rotation period of Arrokoth is similar to those measured for 67P and 103P and falls well within the range measured for the JFC population (62), though JFC rotation is known to be affected by cometary activity (63).

The JFC nuclei listed in table S3 are much darker than Arrokoth, with  $\sim 3$  to  $5$  times smaller geometric albedos. If the JFC nuclei once had higher albedos in their nascent state in the Kuiper belt, then the darkening of their surfaces might be associated with cometary activity while the JFCs are in the inner Solar System. Most surface features on JFC nuclei have been attributed to cometary activity [e.g.,

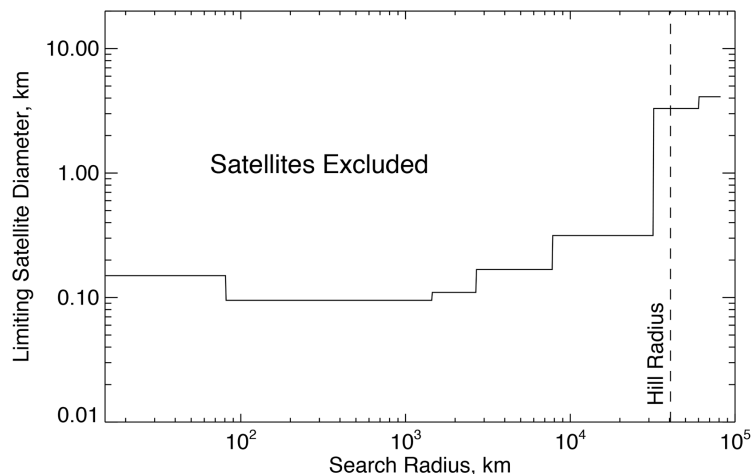


**Fig. 7. Upper limits on possible satellites of Arrokoth.** Excluded regions are plotted as a function of radius from the primary center of mass. The limits assume a satellite with photometric properties similar to those of Arrokoth itself. Gravitationally bound objects must lie within the Hill radius (dashed line), which is calculated assuming Arrokoth has a density of  $500 \text{ kg m}^{-3}$ .

(64, 65)]. Generally, the surfaces of JFC nuclei can be divided into “smooth” and “rough” (or “mottled”) regions, with the rough terrains associated with a preponderance of pits and depressions or mounds and hills (66, 67). The smooth regions of JFCs are generally brighter than average and are often associated with topographic lows, suggesting accumulation by small grains that scatter light more efficiently than the average surface, as we proposed for Arrokoth above. However, on comets, the fallback of grains ejected by sublimation is likely to contribute to smooth terrains (68), and this is less likely to be important on Arrokoth where evidence for sublimation erosion is limited to the pit chains of possible sublimation origin, and tentative evidence for scarp retreat on the small lobe, as mentioned above.

Whereas the large (multikilometer) scale bilobate morphology of Arrokoth is similar to that of four out of the six comets listed in table S3 (see also Fig. 8 and fig. S3), the finer surface textures are not. JFCs imaged at the same resolution as Arrokoth show fewer impact craters than Arrokoth (64), consistent with these comets having highly erosional surfaces. They may lose their surfaces at  $\sim 0.5$  to  $1.0$  m

per orbit (69) with 5- to 10-year orbital periods, so small pits will be removed within a few thousand years. They also show a much rougher surface texture at the 50- to 100-m scale, consistent with sublimation erosion and loss of most of the erosional debris.

### Conclusions

Our dataset from the New Horizons flyby of Arrokoth provides a more complete picture of the physical nature of this object. Images taken on approach show that although both components of Arrokoth are flattened, the flattening is less extreme than initially inferred (1), and the two components have a larger volume ratio,  $1.9 \pm 0.5$ , than previous estimates. Stereo topography and the highest-resolution imaging taken during the flyby show that the large lobe is very flat on the encounter hemisphere. If the large lobe is composed of multiple components that accreted separately, as previously proposed (1), the topographic signature of the boundaries between the components would be expected to be large initially, if the subunits were mechanically similar to the two present lobes at the time of their coming into contact (18). The observed flatness of the large lobe

shows that any such discontinuities have been subdued, and in some cases, eliminated entirely. If subsequent deposition subdued the boundaries, postdepositional processes must be invoked to explain why many of the boundaries are still visible as differences in surface texture or as linear albedo features. Alternatively, the large lobe may be a monolithic body, and the apparent division into subunits may be due entirely to secondary processes. Multiple processes, including impacts, have reworked the surfaces of both lobes after their formation, producing the fissures, small dark hills, and sinuous albedo boundaries seen in the images.

Crater densities on Arrokoth are low but consistent with a surface age of  $>4$  Ga, owing to the expected low cratering rates in the CCKB, even if only craters with the highest confidence of being impact features are included in the counts. This dates the surface as plausibly from the end of Solar System accretion. Crater size–frequency distribution slopes for  $<1$ -km craters on Arrokoth are poorly constrained, but are consistent with the slopes seen for 2- to 15-km craters in the Pluto system (39), suggesting that the shallow size-frequency

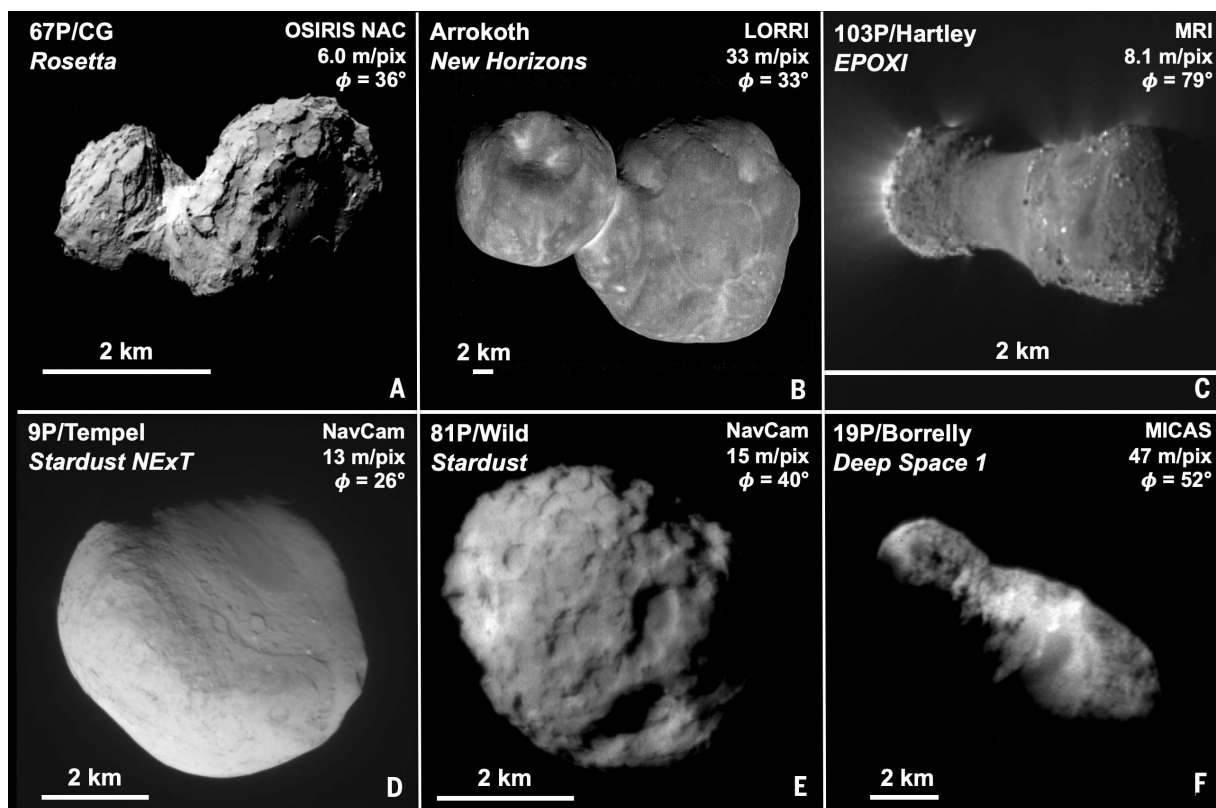


**Fig. 8. Comparison of JFC nuclei to Arrokoth.** The images of JFC nuclei have phase angles similar to those of the highest-resolution image of Arrokoth, except for 103P, which was only observed at much higher phase angles. (A) Rosetta image of 67P/Churyumov–Gerasimenko (73). (B) New Horizons image of Arrokoth (this paper). (C) Extrasolar Planet Observation and Characterization–Deep Impact Extended Investigation (EPOXI) image of

103P/Hartley (74). (D) Stardust image of 9P/Tempel (75). (E) Stardust image of 81P/Wild (76). (F) Deep Space 1 image of 19P/Borrelly (77, 78). [Credit: NASA/JPL] Each frame is scaled so that the body nearly fills it, with the true relative sizes of each body indicated by the scale bars. Arrokoth is much larger than these comets. Figure S3 shows the equivalent images scaled to the same linear resolutions.

distribution for 0.2- to 2-km-diameter KBO impactors (39) may persist down to smaller sizes.

Arrokoth is unlike other small bodies visited by spacecraft. The surfaces of comets are dominated by volatile loss and sublimation erosion driven by the thermal energy inputs, owing to their position in the inner Solar System. The surfaces of asteroids are dominated by high-energy impacts. As a result, asteroid surfaces are primarily rubble or impact ejecta. In both cases, the dominant energy environment (thermal and impact) is driving the surface morphology. Arrokoth's surface is probably a consequence of its presence in the CCKB, where there is much less energy input. The very small relative velocities in this dynamical population result in few impacts, and those that do occur have very slow impact velocities. Without strong energy inputs, either from solar radiation or impacts, we expect the surface of Arrokoth to be dominated by low-level energy inputs from interstellar, solar, and micrometeorite energy sources at slow rates, likely extending to just a few meters' depth (27). It is this low-energy environment that has allowed its surface to be preserved for 4 billion years.

Arrokoth appears to be a typical CCKBO, to the extent that we can compare it to others, so it can be used to understand the cold classical belt as a whole. The bilobed nature of Arrokoth might be common in the Kuiper Belt and could indicate that the bilobed shape of many comet nuclei is a primordial feature. In addition, Arrokoth appears to be a direct product of accretion rather than a collisional fragment and is much smaller than the ~100-km diameter of the break in slope of the size-frequency distribution of CCKBOs (6, 70). These facts are consistent with the break in slope being a primordial feature, as predicted by streaming instability models (71). Arrokoth's appearance is much less consistent with the break in slope being a result of later destruction of small CCKBOs by collisions, a hypothesis also inconsistent with the observed deficit of small craters in the Pluto system (39).

## REFERENCES AND NOTES

- S. A. Stern *et al.*, Initial results from the New Horizons exploration of 2014 MU<sub>69</sub>, a small Kuiper Belt object. *Science* **364**, eaaw9771 (2019). doi: [10.1126/science.aaw9771](https://doi.org/10.1126/science.aaw9771); pmid: [31097641](https://pubmed.ncbi.nlm.nih.gov/31097641/)
- S. B. Porter *et al.*, High-precision orbit fitting and uncertainty analysis of (486958) 2014 MU69. *Astron. J.* **156**, 20 (2018). doi: [10.3847/1538-3881/aac2e1](https://doi.org/10.3847/1538-3881/aac2e1)
- W. M. Grundy *et al.*, Color, composition, and thermal environment of Kuiper Belt object (486958) Arrokoth. *Science* **10.1126/science.aay3705** (2020).
- J.-M. Petit *et al.*, The Canada-France Ecliptic Plane Survey - full data release: The orbital structure of the Kuiper belt. *Astron. J.* **142**, 131 (2011). doi: [10.1088/0004-6256/142/4/131](https://doi.org/10.1088/0004-6256/142/4/131)
- S. Greenstreet, B. Gladman, W. B. McKinnon, J. J. Kavelaars, K. N. Singer, Crater density predictions for New Horizons flyby target 2014 MU69. *Astrophys. J.* **872**, L5 (2019). doi: [10.3847/2041-8213/ab01db](https://doi.org/10.3847/2041-8213/ab01db)
- S. Greenstreet, B. Gladman, W. B. McKinnon, Impact and cratering rates onto Pluto. *Icarus* **258**, 267–288 (2015). doi: [10.1016/j.icarus.2015.05.026](https://doi.org/10.1016/j.icarus.2015.05.026)
- A. F. Cheng *et al.*, Long-Range Reconnaissance Imager on New Horizons. *Space Sci. Rev.* **140**, 189–215 (2008). doi: [10.1007/s11214-007-9271-6](https://doi.org/10.1007/s11214-007-9271-6)
- D. C. Reuter *et al.*, Ralph: A Visible/Infrared Imager for the New Horizons Pluto/Kuiper Belt mission. *Space Sci. Rev.* **140**, 129–154 (2008). doi: [10.1007/s11214-008-9375-7](https://doi.org/10.1007/s11214-008-9375-7)
- Materials and methods are available as supplementary materials.
- S. D. Benecchi *et al.*, The HST lightcurve of (486958) 2014 MU69. *Icarus* **334**, 11–21 (2019). doi: [10.1016/j.icarus.2019.01.023](https://doi.org/10.1016/j.icarus.2019.01.023)
- M. Buie *et al.*, Size and shape constraints of (486958) Arrokoth from stellar occultations (2020). <https://arxiv.org/abs/2001.00125>.
- A. M. Zangari, *et al.*, The mysterious missing light curve of (486958) 2014 MU69, a bi-lobate contact binary visited by New Horizons. *Lunar Planet. Sci. Conf.* 3007 (2019).
- A. Thirouin, S. S. Sheppard, Light curves and rotational properties of the pristine Cold Classical Kuiper Belt objects. *Astron. J.* **157**, 228 (2019). doi: [10.3847/1538-3881/ab18a9](https://doi.org/10.3847/1538-3881/ab18a9)
- S. B. Porter *et al.*, New Horizons distant observations of Cold Classical KBOs. AAS/Division for Planetary Sciences Meeting Abstracts 509.07 (2018).
- A. J. Verbiscer *et al.*, Phase curves from the Kuiper belt: Photometric properties of “distant” KBOs observed by New Horizons. *Astron. J.* **158**, 123 (2019). doi: [10.3847/1538-3881/ab3211](https://doi.org/10.3847/1538-3881/ab3211)
- F. Preusker *et al.*, The global meter-level shape model of comet 67P/Churyumov-Gerasimenko. *Astron. Astrophys.* **607**, L1 (2017). doi: [10.1051/0004-6361/201731798](https://doi.org/10.1051/0004-6361/201731798)
- D. J. Scheeres, *Orbital Motion in Strongly Perturbed Environments: Applications to Asteroids, Comet and Planetary Satellite Orbiters* (Springer-Praxis, Chichester, 2012).
- W. B. McKinnon *et al.*, The solar nebula origin of (486958) Arrokoth, a primordial contact binary in the Kuiper Belt. *Science* **10.1126/science.aay6620** (2020).
- Normal reflectance is the  $I/F$  (where  $I$  is the scattered intensity from the surface and  $\pi F$  is the solar flux at the distance of the scattering surface; also called the bidirectional reflectance) when the incident and emission angles are both zero.
- B. Buratti, J. Veverka, Voyager photometry of Europa. *Icarus* **55**, 93–110 (1983). doi: [10.1016/0019-1035\(83\)90053-2](https://doi.org/10.1016/0019-1035(83)90053-2)
- S. Besse, P. Lamy, L. Jorda, S. Marchi, C. Barbieri, Identification and physical properties of craters on Asteroid (2867) Steins. *Icarus* **221**, 1119–1129 (2012). doi: [10.1016/j.icarus.2012.08.008](https://doi.org/10.1016/j.icarus.2012.08.008)
- M. S. Robinson, P. C. Thomas, J. Veverka, S. L. Murchie, B. B. Wilcox, The geology of 433 Eros. *Meteorit. Planet. Sci.* **37**, 1651–1684 (2002). doi: [10.1111/j.1945-5100.2002.tb01157.x](https://doi.org/10.1111/j.1945-5100.2002.tb01157.x)
- L. Prockter *et al.*, Surface expressions of structural features on Eros. *Icarus* **155**, 75–93 (2002). doi: [10.1006/icar.2001.6770](https://doi.org/10.1006/icar.2001.6770)
- D. L. Buczkowski, O. S. Barnouin-Jha, L. M. Prockter, 433 Eros lineaments: Global mapping and analysis. *Icarus* **193**, 39–52 (2008). doi: [10.1016/j.icarus.2007.06.028](https://doi.org/10.1016/j.icarus.2007.06.028)
- S. J. Morrison, P. C. Thomas, M. S. Tiscareno, J. A. Burns, J. Veverka, Grooves on small Saturnian satellites and other objects: Characteristics and significance. *Icarus* **204**, 262–270 (2009). doi: [10.1016/j.icarus.2009.06.003](https://doi.org/10.1016/j.icarus.2009.06.003)
- T. A. Hurford *et al.*, Tidal disruption of Phobos as the cause of surface fractures. *J. Geophys. Res. Planets* **121**, 1054–1065 (2016). doi: [10.1002/2015JE004943](https://doi.org/10.1002/2015JE004943)
- S. A. Stern, The evolution of comets in the Oort cloud and Kuiper belt. *Nature* **424**, 639–642 (2003). doi: [10.1038/nature01725](https://doi.org/10.1038/nature01725); pmid: [12904784](https://pubmed.ncbi.nlm.nih.gov/12904784/)
- M. J. S. Belton *et al.*, The internal structure of Jupiter family cometary nuclei from Deep Impact observations: The “talps” or “layered pile” model. *Icarus* **187**, 332–344 (2007). doi: [10.1016/j.icarus.2006.09.005](https://doi.org/10.1016/j.icarus.2006.09.005)
- M. Jutzi, E. Asphaug, The shape and structure of cometary nuclei as a result of low-velocity accretion. *Science* **348**, 1355–1358 (2015). doi: [10.1126/science.aaa4747](https://doi.org/10.1126/science.aaa4747); pmid: [26022415](https://pubmed.ncbi.nlm.nih.gov/26022415/)
- K. R. Housen, W. J. Sweet, K. A. Holsapple, Impacts into porous asteroids. *Icarus* **300**, 72–96 (2018). doi: [10.1016/j.icarus.2017.08.019](https://doi.org/10.1016/j.icarus.2017.08.019)
- S. J. Robbins *et al.*, Measuring impact crater depth throughout the solar system. *Meteorit. Planet. Sci.* **53**, 583–637 (2018). doi: [10.1111/maps.12956](https://doi.org/10.1111/maps.12956)
- K. A. Holsapple, K. R. Housen, A crater and its ejecta: An interpretation of Deep Impact. *Icarus* **191**, 586–597 (2007). doi: [10.1016/j.icarus.2006.08.035](https://doi.org/10.1016/j.icarus.2006.08.035)
- D. Nesvorný, Dynamical evolution of the early Solar System. *Annu. Rev. Astron. Astrophys.* **56**, 137–174 (2018). doi: [10.1146/annurev-astro-081817-052028](https://doi.org/10.1146/annurev-astro-081817-052028)
- S. Sugita *et al.*, The geomorphology, color, and thermal properties of Ryugu: Implications for parent-body processes. *Science* **364**, eaaw0422 (2019). doi: [10.1126/science.aaw0422](https://doi.org/10.1126/science.aaw0422); pmid: [30890587](https://pubmed.ncbi.nlm.nih.gov/30890587/)
- K. J. Walsh *et al.*, Craters, boulders and regolith of (101955) Bennu. *Nat. Geosci.* **12**, 242–246 (2019). doi: [10.1038/s41561-019-0326-6](https://doi.org/10.1038/s41561-019-0326-6)
- D. J. Scheeres *et al.*, The dynamic geophysical environment of (101955) Bennu based on OSIRIS-REx measurements. *Nat. Astron.* **3**, 352–361 (2019). doi: [10.1038/s41550-019-0721-3](https://doi.org/10.1038/s41550-019-0721-3)
- A. H. Parker, The intrinsic Neptune Trojan orbit distribution: Implications for the primordial disk and planet migration. *Icarus* **247**, 112–125 (2015). doi: [10.1016/j.icarus.2014.09.043](https://doi.org/10.1016/j.icarus.2014.09.043)
- S. Mazrouei, R. R. Ghent, W. F. Bottke, A. H. Parker, T. M. Gernon, Earth and Moon impact flux increased at the end of the Paleozoic. *Science* **363**, 253–257 (2019). doi: [10.1126/science.aar4058](https://doi.org/10.1126/science.aar4058); pmid: [30655437](https://pubmed.ncbi.nlm.nih.gov/30655437/)
- K. N. Singer *et al.*, Impact craters on Pluto and Charon indicate a deficit of small Kuiper belt objects. *Science* **363**, 955–959 (2019). doi: [10.1126/science.aap8628](https://doi.org/10.1126/science.aap8628); pmid: [30819958](https://pubmed.ncbi.nlm.nih.gov/30819958/)
- K. S. Noll, W. M. Grundy, D. Nesvorný, A. Thirouin, “Transneptunian binaries” in *The Trans-Neptunian Solar System*, D. Prialnik, M. A. Barucci, L. Young, Eds. (Elsevier, 2019), pp. 205–224.
- W. R. Johnston, Binary Minor Planets Compilation V3.0. urn: nasa:pds:ast\_binary\_parameters\_compilation:3.0. NASA Planetary Data System, (2019). <https://sbn.psi.edu/pds/resource/binmp.html>.
- F. Marchis *et al.*, The puzzling mutual orbit of the binary Trojan asteroid (624) Hektor. *Astrophys. J.* **783**, L37 (2014). doi: [10.1088/2041-8205/783/2/L37](https://doi.org/10.1088/2041-8205/783/2/L37)
- P. Descamps *et al.*, Triplicity and physical characteristics of Asteroid (216) Kleopatra. *Icarus* **211**, 1022–1033 (2011). doi: [10.1016/j.icarus.2010.11.016](https://doi.org/10.1016/j.icarus.2010.11.016)
- F. Braga-Ribas *et al.*, A ring system detected around the Centaur (10199) Chariklo. *Nature* **508**, 72–75 (2014). doi: [10.1038/nature13155](https://doi.org/10.1038/nature13155); pmid: [24670644](https://pubmed.ncbi.nlm.nih.gov/24670644/)
- J. L. Ortiz *et al.*, The size, shape, density and ring of the dwarf planet Haumea from a stellar occultation. *Nature* **550**, 219–223 (2017). doi: [10.1038/nature24051](https://doi.org/10.1038/nature24051); pmid: [29022593](https://pubmed.ncbi.nlm.nih.gov/29022593/)
- J. L. Ortiz *et al.*, Possible ring material around centaur (2060) Chiron. *Astron. Astrophys.* **576**, A18 (2015). doi: [10.1051/0004-6361/201424461](https://doi.org/10.1051/0004-6361/201424461)
- H. B. Throop *et al.*, The Jovian rings: New results derived from Cassini, Galileo, Voyager, and Earth-based observations. *Icarus* **172**, 59–77 (2004). doi: [10.1016/j.icarus.2003.12.020](https://doi.org/10.1016/j.icarus.2003.12.020)
- T. R. Lauer *et al.*, The New Horizons and Hubble Space Telescope search for rings, dust, and debris in the Pluto-Charon system. *Icarus* **301**, 155–172 (2018). doi: [10.1016/j.icarus.2017.09.033](https://doi.org/10.1016/j.icarus.2017.09.033)
- M. Horányi *et al.*, The Student Dust Counter on the New Horizons Mission. *Space Sci. Rev.* **140**, 387–402 (2008). doi: [10.1007/s11214-007-9250-y](https://doi.org/10.1007/s11214-007-9250-y)
- P. Lacerda *et al.*, The albedo-color diversity of transneptunian objects. *Astrophys. J.* **793**, L2 (2014). doi: [10.1088/2041-8205/793/L2](https://doi.org/10.1088/2041-8205/793/L2)
- A. Thirouin, S. S. Sheppard, The Plutino population: An abundance of contact binaries. *Astron. J.* **155**, 248 (2018). doi: [10.3847/1538-3881/aac0ff](https://doi.org/10.3847/1538-3881/aac0ff)
- P. Thomas, J. Veverka, J. Helfenstein, Voyager observations of Nereid. *J. Geophys. Res.* **96** (S01), 19253 (1991). doi: [10.1029/91JA01735](https://doi.org/10.1029/91JA01735)
- T. V. Johnson, J. I. Lunine, Saturn's moon Phoebe as a captured body from the outer Solar System. *Nature* **435**, 69–71 (2005). doi: [10.1038/nature03384](https://doi.org/10.1038/nature03384); pmid: [15875015](https://pubmed.ncbi.nlm.nih.gov/15875015/)
- W. K. Hartmann, A satellite-asteroid mystery and a possible early flux of scattered C-class asteroids. *Icarus* **71**, 57–68 (1987). doi: [10.1016/0019-1035\(87\)90162-X](https://doi.org/10.1016/0019-1035(87)90162-X)
- J. Castillo-Rogez, P. Vernazza, K. Walsh, Geophysical evidence that Saturn's Moon Phoebe originated from a C-type asteroid reservoir. *Mon. Not. R. Astron. Soc.* **486**, 538–543 (2019). doi: [10.1093/mnras/stz786](https://doi.org/10.1093/mnras/stz786)
- D. P. Simonelli *et al.*, Phoebe: Albedo map and photometric properties. *Icarus* **138**, 249–258 (1999). doi: [10.1006/icar.1999.6077](https://doi.org/10.1006/icar.1999.6077)
- B. J. Buratti, M. D. Hicks, K. A. Tryka, M. S. Sittig, R. L. Newburn, High-resolution 0.33–0.92 mm spectra of

- Iapetus, Hyperion, Phoebe, Rhea, Dione, and D-type asteroids: How are they related? *Icarus* **155**, 375–381 (2002). doi: [10.1006/icar.2001.6730](https://doi.org/10.1006/icar.2001.6730)
58. C. C. Porco *et al.*, Cassini Imaging Science: Initial results on Phoebe and Iapetus. *Science* **307**, 1237–1242 (2005). doi: [10.1126/science.1107981](https://doi.org/10.1126/science.1107981); pmid: [15731440](https://pubmed.ncbi.nlm.nih.gov/15731440/)
59. M. Duncan, H. Levison, L. Dones, “Dynamical evolution of ecliptic comets”. In *Comets II*, M. C. Festou, H. U. Keller, H. A. Weaver Eds. (University of Arizona Press, Tucson, 193, 2004).
60. D. E. Vavilov, S. Eggel, Y. D. Medvedev, P. B. Zatitskiy, Shape evolution of cometary nuclei via anisotropic mass loss. *Astron. Astrophys.* **622**, L5 (2019). doi: [10.1051/0004-6361/201834806](https://doi.org/10.1051/0004-6361/201834806)
61. O. Groussin *et al.*, The thermal, mechanical, structural, and dielectric properties of cometary nuclei after Rosetta. *Space Sci. Rev.* **215**, 29 (2019). doi: [10.1007/s11214-019-0594-x](https://doi.org/10.1007/s11214-019-0594-x)
62. R. Kokotanekova *et al.*, Rotation of cometary nuclei: New light curves and an update of the ensemble properties of Jupiter-family comets. *Mon. Not. R. Astron. Soc.* **471**, 2974–3007 (2017). doi: [10.1093/mnras/stx1716](https://doi.org/10.1093/mnras/stx1716)
63. D. Bodewits, T. L. Farnham, M. S. P. Kelley, M. M. Knight, A rapid decrease in the rotation rate of comet 41P/Tuttle-Giacobini-Kresák. *Nature* **553**, 186–188 (2018). doi: [10.1038/nature25150](https://doi.org/10.1038/nature25150); pmid: [29323296](https://pubmed.ncbi.nlm.nih.gov/29323296/)
64. J. Sunshine, N. Thomas, M. R. El-Maarry, T. L. Farnham, Evidence for geologic processes on comets. *J. Geophys. Res. Planets* **121**, 2194–2210 (2016). doi: [10.1002/2016JE005119](https://doi.org/10.1002/2016JE005119)
65. M. R. El-Maarry *et al.*, Surface changes on comet 67P/Churyumov-Gerasimenko suggest a more active past. *Science* **355**, 1392–1395 (2017). doi: [10.1126/science.aak9384](https://doi.org/10.1126/science.aak9384); pmid: [28325842](https://pubmed.ncbi.nlm.nih.gov/28325842/)
66. P. C. Thomas *et al.*, Shape, density, and geology of the nucleus of Comet 103P/Hartley 2. *Icarus* **222**, 550–558 (2013). doi: [10.1016/j.icarus.2012.05.034](https://doi.org/10.1016/j.icarus.2012.05.034)
67. D. T. Britt *et al.*, The morphology and surface processes of Comet 19/P Borrelly. *Icarus* **167**, 45–53 (2004). doi: [10.1016/j.icarus.2003.09.004](https://doi.org/10.1016/j.icarus.2003.09.004)
68. N. Thomas *et al.*, Redistribution of particles across the nucleus of comet 67P/Churyumov-Gerasimenko. *Astron. Astrophys.* **583**, A17 (2015). doi: [10.1051/0004-6361/201526049](https://doi.org/10.1051/0004-6361/201526049)
69. D. Prrialnik, J. Benkhoff, M. Podolak, “Modeling the structure and activity of comet nuclei” in *Comets II*, M. C. Festou, H. U. Keller, H. A. Weaver Eds. (Univ. of Arizona Press, Tucson, 2004), pp. 359–387.
70. W. C. Fraser, M. E. Brown, A. Morbidelli, A. Parker, K. Batygin, The absolute magnitude distribution of Kuiper Belt Objects. *Astrophys. J.* **782**, 100 (2014). doi: [10.1088/0004-637X/782/2/100](https://doi.org/10.1088/0004-637X/782/2/100)
71. R. Li, A. N. Youdin, J. B. Simon, Demographics of planetesimals formed by the streaming instability. *Astrophys. J.* **885**, 69 (2019). doi: [10.3847/1538-4357/ab480d](https://doi.org/10.3847/1538-4357/ab480d)
72. H. J. Melosh, *Impact Cratering: A Geologic Process* (Oxford Univ. Press, Oxford, 1989).
73. H. Sierks *et al.*, On the nucleus structure and activity of comet 67P/Churyumov-Gerasimenko. *Science* **347**, aaa1044 (2015). doi: [10.1126/science.aaa1044](https://doi.org/10.1126/science.aaa1044); pmid: [25613897](https://pubmed.ncbi.nlm.nih.gov/25613897/)
74. M. F. A'Hearn *et al.*, EPOXI at comet Hartley 2. *Science* **332**, 1396–1400 (2011). doi: [10.1126/science.1204054](https://doi.org/10.1126/science.1204054); pmid: [21680835](https://pubmed.ncbi.nlm.nih.gov/21680835/)
75. J. Veverka *et al.*, Return to Comet Tempel 1: Overview of Stardust-NExT results. *Icarus* **222**, 424–435 (2013). doi: [10.1016/j.icarus.2012.03.034](https://doi.org/10.1016/j.icarus.2012.03.034)
76. D. E. Brownlee *et al.*, Surface of young Jupiter family comet 81P/Wild 2: View from the Stardust Spacecraft. *Science* **304**, 1764–1769 (2004). doi: [10.1126/science.1097899](https://doi.org/10.1126/science.1097899); pmid: [15205524](https://pubmed.ncbi.nlm.nih.gov/15205524/)
77. L. A. Soderblom *et al.*, Observations of comet 19P/Borrelly by the miniature integrated camera and spectrometer aboard Deep Space 1. *Science* **296**, 1087–1091 (2002). doi: [10.1126/science.1069527](https://doi.org/10.1126/science.1069527); pmid: [11934989](https://pubmed.ncbi.nlm.nih.gov/11934989/)
78. B. J. Buratti *et al.*, Deep Space 1 photometry of the nucleus of Comet 19P/Borrelly. *Icarus* **167**, 16–29 (2004). doi: [10.1016/j.icarus.2003.05.002](https://doi.org/10.1016/j.icarus.2003.05.002)
79. J. R. Spencer *et al.*, Data archive for Spencer *et al.* 2020, The geology and geophysics of Kuiper Belt object (486958) Arrokoth, Science, figshare (2020); <https://doi.org/10.6084/m9.figshare.11485443>.

#### ACKNOWLEDGMENTS

We thank all who contributed to the success of the New Horizons flyby of Arrokoth, and in particular the National Astronomical Observatory of Japan's Subaru Telescope, the Carnegie Observatory's Magellan Telescopes, the Canada-France-Hawaii Telescope, the NASA Hubble Space Telescope, the Harvard-Smithsonian Center for Astrophysics, the Massachusetts Institute of Technology, Northern Arizona University, the University of Hawaii, the Hertzberg Institute for

Astrophysics, and NASA, for their support of the search campaign that led to its discovery. We also are indebted to the Hubble Space Telescope and the European Space Agency's Gaia mission for their key roles in the precise orbit determination required to enable the successful flyby.

**Funding:** Supported by NASA's New Horizons project under contracts NASW-02008 and NAS5-97271/TaskOrder30. J.J.K. was supported by the National Research Council of Canada and the National Science and Engineering Research Council of Canada. **Author contributions:** The primary contributors to each section were as follows: Stereo and shape modeling: S.B.P., R.A.B., P.M.S., A.M.Z., M.W.B., and T.R.L. Geophysical analysis: J.T.K., O.M.U., and W.B.M. Photometric analysis: B.J.B., J.D.H., A.J.V., and S.D.B. Geological mapping and interpretation: J.M.M., O.L.W., R.A.B., O.M.U., J.R.S., and T.R.L. Crater analysis: K.N.S., S.J.R., K.D.R., P.M.S., and A.H.P. Satellite and ring search: J.R.S., S.B.P., M.W.B., M.R.S., T.R.L., H.B.T., A.J.V., A.M.Z., W.M.G., D.P.H., E.B., and D.E.K. Astronomical context: H.A.W., D.T.B., C.M.L., M.R.E.-M., J.J.K., and W.B.M. Paper compilation and synthesis: J.R.S. S.A.S. is the principal investigator of the New Horizons mission and reviewed this manuscript. All other authors participated in mission planning, initial discovery and tracking of Arrokoth, science data reduction or analysis, or provided inputs and critique to this manuscript.

**Competing interests:** The authors declare no competing interests.

**Data and materials availability:** All images, spacecraft data, and the shape model used in this paper are available at figshare (79). Additional fully calibrated New Horizons Arrokoth data and higher-order data products will be released by the NASA Planetary Data System in a series of stages in 2020 and 2021, owing to the time required to fully downlink and calibrate the dataset.

#### SUPPLEMENTARY MATERIALS

[science.sciencemag.org/content/367/6481/eaay3999/suppl/DC1](https://science.sciencemag.org/content/367/6481/eaay3999/suppl/DC1)  
Materials and Methods  
Supplementary Text  
Figs. S1 to S4  
Tables S1 to S3  
References (80–90)  
Data S1 to S3

14 June 2019; accepted 27 January 2020

Published online 13 February 2020

[10.1126/science.aay3999](https://doi.org/10.1126/science.aay3999)

## The geology and geophysics of Kuiper Belt object (486958) Arrokoth

J. R. Spencer, S. A. Stern, J. M. Moore, H. A. Weaver, K. N. Singer, C. B. Olkin, A. J. Verbiscer, W. B. McKinnon, J. Wm. Parker, R. A. Beyer, J. T. Keane, T. R. Lauer, S. B. Porter, O. L. White, B. J. Buratti, M. R. El-Maarry, C. M. Lisse, A. H. Parker, H. B. Throop, S. J. Robbins, O. M. Umurhan, R. P. Binzel, D. T. Britt, M. W. Buie, A. F. Cheng, D. P. Cruikshank, H. A. Elliott, G. R. Gladstone, W. M. Grundy, M. E. Hill, M. Horanyi, D. E. Jennings, J. J. Kavelaars, I. R. Linscott, D. J. McComas, R. L. McNutt Jr., S. Protopapa, D. C. Reuter, P. M. Schenk, M. R. Showalter, L. A. Young, A. M. Zangari, A. Y. Abedin, C. B. Beddingfield, S. D. Benecchi, E. Bernardoni, C. J. Bierson, D. Borncamp, V. J. Bray, A. L. Chaikin, R. D. Dhringra, C. Fuentes, T. Fuse, P. L. Gay, S. D. J. Gwyn, D. P. Hamilton, J. D. Hofgartner, M. J. Holman, A. D. Howard, C. J. A. Howett, H. Karoji, D. E. Kaufmann, M. Kinczyk, B. H. May, M. Mountain, M. Pätzold, J. M. Petit, M. R. Piquette, I. N. Reid, H. J. Reitsema, K. D. Runyon, S. S. Sheppard, J. A. Stansberry, T. Stryk, P. Tanga, D. J. Tholen, D. E. Trilling and L. H. Wasserman

*Science* **367** (6481), eaay3999.

DOI: 10.1126/science.aay3999originally published online February 13, 2020

### Examining Arrokoth

The New Horizons spacecraft flew past the Kuiper Belt object (486958) Arrokoth (also known as 2014 MU<sub>69</sub>) in January 2019. Because of the great distance to the outer Solar System and limited bandwidth, it will take until late 2020 to downlink all the spacecraft's observations back to Earth. Three papers in this issue analyze recently downlinked data, including the highest-resolution images taken during the encounter (see the Perspective by Jewitt). Spencer *et al.* examined Arrokoth's geology and geophysics using stereo imaging, dated the surface using impact craters, and produced a geomorphological map. Grundy *et al.* investigated the composition of the surface using color imaging and spectroscopic data and assessed Arrokoth's thermal emission using microwave radiometry. McKinnon *et al.* used simulations to determine how Arrokoth formed: Two gravitationally bound objects gently spiraled together during the formation of the Solar System. Together, these papers determine the age, composition, and formation process of the most pristine object yet visited by a spacecraft.

*Science*, this issue p. eaay3999, p. eaay3705, p. eaay6620; see also p. 980

#### ARTICLE TOOLS

<http://science.sciencemag.org/content/367/6481/eaay3999>

#### SUPPLEMENTARY MATERIALS

<http://science.sciencemag.org/content/suppl/2020/02/12/science.aay3999.DC1>

#### RELATED CONTENT

<http://science.sciencemag.org/content/sci/367/6481/eaay3705.full>  
<http://science.sciencemag.org/content/sci/367/6481/eaay6620.full>

#### REFERENCES

This article cites 85 articles, 14 of which you can access for free  
<http://science.sciencemag.org/content/367/6481/eaay3999#BIBL>

Use of this article is subject to the [Terms of Service](#)

---

*Science* (print ISSN 0036-8075; online ISSN 1095-9203) is published by the American Association for the Advancement of Science, 1200 New York Avenue NW, Washington, DC 20005. The title *Science* is a registered trademark of AAAS.

Copyright © 2020 The Authors, some rights reserved; exclusive licensee American Association for the Advancement of Science. No claim to original U.S. Government Works

PERMISSIONS

<http://www.sciencemag.org/help/reprints-and-permissions>

Use of this article is subject to the [Terms of Service](#)

---

*Science* (print ISSN 0036-8075; online ISSN 1095-9203) is published by the American Association for the Advancement of Science, 1200 New York Avenue NW, Washington, DC 20005. The title *Science* is a registered trademark of AAAS.

Copyright © 2020 The Authors, some rights reserved; exclusive licensee American Association for the Advancement of Science. No claim to original U.S. Government Works